Computer Methods in Applied Mechanics and Engineering 423 (2024) 116872

Contents lists available at ScienceDirect

Comput. Methods Appl. Mech. Engrg.

journal homepage: www.elsevier.com/locate/cma

An extended isogeometric boundary element formulation for three-dimensional linear elastic fracture mechanics

Matheus Rocha [a,b,*], Jon Trevelyan [b], Edson Denner Leonel [a]

[a] Department of Structural Engineering, São Carlos School of Engineering, University of São Paulo, Av. Trabalhador São Carlense, 400, São Carlos, 13566-590, São Paulo, Brazil

[b] Department of Engineering, Durham University, South Road, Durham, DH1 3LE, United Kingdom

ARTICLE INFO

Keywords:
Extended isogeometric boundary element method
Enriched formulations
Three-dimensional fracture mechanics
Linear elastic fracture mechanics
Stress intensity factors

ABSTRACT

This paper presents a novel extended isogeometric boundary element formulation (XIGABEM) for three-dimensional linear elastic fracture mechanics. The formulation utilises the Dual BEM to accommodate coincident geometries for opposing crack surfaces, and inherits the well-known advantages of the NURBS basis as other isogeometric implementations. The originality herein involves the extension of the above-mentioned scheme to 3D using enrichment functions derived from asymptotic solutions for near-field crack tip displacements, in which Williams' expansions are used on the crack surfaces and on the boundaries crossed by the crack front. Besides, Heaviside functions enrich external boundaries and allow the displacement discontinuity modelling. As with most enriched formulations, additional degrees of freedom are introduced; novel strategies are presented for the generation of auxiliary equations to recover a square system.

Another key element of the proposed scheme is that the stress intensity factors are recovered directly from the solution vector and no post processing is required. Four applications demonstrate the formulation robustness, with results of models having comparatively few degrees of freedom comparing well against classical and other published results.

1. Introduction

The correct prediction of the mechanical behaviour of cracked materials and structures is of great interest to engineers owing to the influence of cracks on material failure mechanisms. Fracture is a severe mode of failure because it can occur suddenly and catastrophically, often without warning. In studying crack behaviour, Linear Elastic Fracture Mechanics (LEFM) provides a method of assessment for problems in which the fracture process zone (FPZ) is negligible. The assumption that the plastic region arising at a crack tip is small is often valid for brittle materials, hydraulic fracture and for linear fatigue life cycle analysis, for instance. There exist several examples of numerical analysis formulations (some of them enriched) for planar components under the LEFM assumption, and this is satisfactory for the assessment of cracks in plane structures. However, some industry sectors involve mechanical components that require a fully three-dimensional formulation to represent their mechanical fields. Therefore, there is a need for effective and accurate numerical formulations capable of determining the response of these three-dimensional bodies considering LEFM, which can contribute to safe and economic design.

* Corresponding author at: Department of Structural Engineering, São Carlos School of Engineering, University of São Paulo, Av. Trabalhador São Carlense, 400, São Carlos, 13566-590, São Paulo, Brazil.
E-mail address: rocha.matheus@usp.br (M. Rocha).

https://doi.org/10.1016/j.cma.2024.116872
Received 27 December 2023; Received in revised form 19 February 2024; Accepted 20 February 2024
Available online 26 February 2024
0045-7825/© 2024 Elsevier B.V. All rights reserved.

The crack stability criteria in the LEFM demand the computation of stress intensity factors (SIFs) that characterise the complexity of the crack tip stress field. In a numerical analysis, such as those based on finite elements or boundary elements, it typically requires specific techniques that accommodate the singular behaviour of the stress field. J integral methods [1–3] are path-independent, precise approaches, in which a closed contour integral is performed around the crack tip to assess the SIFs. However, in three-dimensional approaches, this task becomes computationally prohibiting. Other methods, such as the Displacement Correlation Technique [4] and special crack tip elements [5], can be applied, however, with lower accuracy.

The Finite Element Method (FEM) is the most widespread numerical method for the solution of elasticity problems. Classical FEM formulations assume the displacement to be represented using polynomial functions, so they struggle in representing the singular stress field at the crack tip. Another drawback of the finite element approach is the requirement of a complex and time-consuming re-meshing at each crack growth step for this type of analysis. On the other hand, alternative numerical approaches arise to successfully circumvent these problems, such as peridynamics [6–9] and phase-field models [10–12]. The comparison between these two methods performed by Dielh et al. [13] highlights as advantages of both methods: ability to capture crack initiation, the dismissal of an additional criterion to describe crack growth and their applicability in multi-field fracture. However, these two methods are computationally expensive and, as a plausible consequence, there are few three-dimensional researches based on these two approaches. Moreover, the peridynamics approach can allow mechanical effects to propagate too quickly through media since mechanical interactions are instantaneous over a finite horizon.

Efforts to overcome the limitations of describing a singular stress field using polynomials led to the development of the eXtended/Generalized Finite Element Method (XFEM/GFEM). In this approach, the displacement is expanded in a set of functions drawn from an *a priori* known expected behaviour in the response. The implementation in existing FEM codes is relatively straightforward since these additional functions generate only an augmented algebraic system while preserving the standard FEM contribution. The introduction of the Williams solution [14] (according to Aragón and Duarte [15]) and the discontinuous (Heaviside) [16] functions in the approximation space of the two-dimensional XFEM/GFEM allows the crack to exist and propagate in a geometry completely independently of the FEM mesh. The seminal work of Sukumar et al. [17] incorporated these enrichment functions for three-dimensional analysis. Based on these strategies, several applications of the XFEM/GFEM were successful for fracture mechanics problems, such as in dynamic crack propagation [18], higher order functions in XFEM/GFEM [19], crack initiation [20], among others [21–24]. Moreover, XFEM/GFEM obtains optimal convergence in LEFM problems in both 2-D [19,25–28] and 3-D [29,30] applications. However, it is important to use techniques such as these with caution because of the consequent ill-conditioning in the stiffness matrix caused by the enrichment contributions, which can compromise solution accuracy if not suitably treated.

The Boundary Element Method (BEM) has become popular as a robust approach for LEFM problems. The advantages of the BEM arise from the boundary-only mesh requirement, which allows a straightforward introduction of the crack and also simplifies the re-meshing process during crack propagation. The reduction of the problem dimensionality simplifies the mesh generation task. Another advantage of the BEM in the fracture mechanics is the absence of domain interpolation, which permits an accurate determination of the mechanical fields even close to the crack tip despite the singular behaviour at this region. The dual BEM formulation [31] allows the BEM to be used effectively for fractured media. This strategy consists of using two linearly independent boundary equations, one at each of the opposing crack faces, overcoming the singularity in the algebraic system. Due to the these characteristics, the BEM has been successfully explored for two-dimensional crack problems [32–36], and also for three-dimensional applications [37–41]. In the three-dimensional context, there are some strong singularities and hyper-singularities that demand semi-analytical treatment, as presented in [42,43].

In contrast to the wide body of literature in the XFEM/GFEM, the use of enrichment functions to extend BEM approximations is comparatively in its infancy. The pioneering works of Simpson and Trevelyan [44,45] utilised the concept of Partition of Unity to expand the displacement field with the Williams solution for displacements in two-dimensional fracture problems, resulting in highly accurate stress intensity factor solutions from coarse models. Besides, the availability of SIFs directly from the solution vector, with any post-processing cost, is a considerable advantage. This has been demonstrated for 2-D isotropic [46] and anisotropic [47] media. In addition, a Heaviside enrichment function for 2-D LEFM problems [48] in the XBEM dismisses the re-meshing task when the crack intersects the external boundary. Once the crossing in this case is a point-line intersection, the re-meshing would not be as cumbersome as in 3-D applications. The sole study considering 3-D XBEM [49] introduces the direct extraction of SIF by the Williams solution for displacements, in which only the analysis of non-inclined cracks is present. Therefore, the proposition of enrichment functions for three-dimensional extended BEM formulations is a novel aspect that is the main objective of this work.

Recently, since the proposition of the Isogeometric Analysis (IGA) by Hughes et al. [50], this paradigm has increasingly become a powerful tool in the numerical methods context. By applying the approximation functions of Computer-Aided Design (CAD) geometries, the numerical methods inherit several improvements. The approximation functions can possess a high degree of continuity, which allows the exact representation of complex curves as circles and ellipses. Another improvement relies on the direct use of the CAD geometry as the mesh, which can minimise one of the most demanding tasks of industrial structural analysis. Further, there is a large body of literature showing that the smoothness and non-negativity of the IGA basis functions frequently gives improved convergence properties over the classical piece-wise polynomial approximation space. The use of IGA for fracture mechanics has been widely explored, in which phase-field modelling [51–53] and the eXtended IGA (XIGA) approach [54–59] demonstrate the robustness of using IGA basis functions on Finite Element procedures.

In the BEM framework, the IGA concept becomes even more appealing because the CAD geometry mesh, which is purely a surface in 3-D models, is directly the boundary-only mesh. In elasto-statics, the IGABEM starts with the work of Simpson et al. for 2-D applications [60], while Scott et al. [61] extend this framework for 3-D geometries by using unstructured T-splines. Beer et al. [62]

present the foundations of the IGABEM, as well as its application in a plethora of engineering problems. The use of enrichment functions in 2-D IGABEM also permitted the direct extraction of LEFM relevant parameters, such as SIFs in homogeneous media [63], and SIFs and T-stresses for bi-materials [64]. It is relevant to mention that these enriched approaches align with the Geometry Independent Field approximaTion (GIFT) paradigm [65], firstly introduced by Marussig et al. [66] for elasticity applications with IGABEM. This strategy consists of using a different set of approximation functions in the geometry and in the approximation fields. As a consequence, it becomes possible to refine the mechanical fields without changing the geometry. Following studies have shown the advantages of GIFT for 2-D and 3-D elasto-statics [67–69], fluid mechanics [70], and potential problems [71] in the BEM framework.

For three-dimensional fracture mechanics, the IGABEM has been successfully applied by Peng et al. [72] and further explored as in [73–76]. Still, in all these works the boundary element formulation gives a non-physical displacement jump at the crack tip so that, although the J-integral can provide good SIFs, the local displacement field is incorrectly represented. Moreover, the IGABEM demands a mesh alignment between the external boundary and the crack mesh to allow the numerical method to capture the correspondent discontinuous field. However, this can lead to a re-meshing procedure that may be impractical for NURBS surfaces, once they are based on a tensor-product of two uni-variate NURBS curves, which represent a large portion of the solid.

In this study we present for the first time a XIGABEM formulation for three-dimensional LEFM problems capable of directly extracting SIFs, reducing the errors on the mechanical fields description at the crack front, dismissing the requirement for mesh alignment at the intersection between crack and external boundary, and also improving the convergence rate. These capabilities derive from the use of three different types of enrichment functions: (i) over fully cut external boundary meshes a Heaviside function is introduced to account for the discontinuity in the displacement field, (ii) over partially intersected boundary faces the leading order term in the Williams solution is used to capture both the displacement discontinuity across opposing crack faces and also the $\sqrt{r}$ behaviour observed in the displacement field, (iii) over the crack surfaces themselves an enrichment also based on the Williams solution allows the introduction of the SIFs as system unknowns in the main BEM solution vector. Another advantage of these novel formulations, as in the XFEM/GFEM, is the possibility of their coupling to existing IGABEM codes without changes in the existing influence matrices.

This work is organised in the following manner. Section 2 defines the enrichment functions and how they are incorporated in the IGABEM framework, with a remark on the additional equations required to generate a square system. Next, Section 3 discusses some specific implementation aspects required by the enrichment function. Then, Section 4 presents four LEFM numerical applications demonstrating the improvements of the XIGABEM when compared against the standard IGABEM framework.

2. Enrichment strategies on 3-D IGABEM for fracture mechanics

This section discusses the enrichment schemes adopted in the proposed extended IGABEM for linear elastic fracture mechanics. It constitutes several advances in the well-established IGABEM formulation for three-dimensional elasto-statics, which is presented in Appendix A.

2.1. Heaviside enrichment for strong discontinuities

As well understood in eXtended Finite Element Method (XFEM) research, a Heaviside function is useful to represent strong discontinuities in the displacement field for fully intersected boundaries. Once NURBS surfaces represent large portions of the discretised domain, it becomes complex or even unfeasible to align a mesh given by a CAD model with an intersecting edge crack. Therefore, this enrichment allows strong discontinuities on these cut surfaces to be captured successfully without re-meshing. In this approach, the standard IGABEM displacement field, Eq. (A.7), expands in a manner as follows:

$$u_k^{\gamma}(\xi_1,\xi_2) = \sum_{\alpha=1}^{n^{\gamma}} \phi_{\alpha}^{\gamma}(\xi_1,\xi_2) d_k^{\beta} + \sum_{\alpha=1}^{n_{\mathscr{H}}^{\gamma}} \left[\mathscr{H}(\xi_1,\xi_2) - \mathscr{H}_{\alpha}\right] \phi_{\alpha}^{\gamma\mathscr{H}} \overline{d}_k^{\beta} \tag{1}$$

where $u_k^{\gamma}(\xi_1,\xi_2)$ is the displacement at the enriched NURBS surface $\gamma^{\mathscr{H}}$. $\mathscr{H}$ represents the Heaviside function, which takes the value -1.0 before the crossing and 1.0 after it. $\mathscr{H}_{\alpha}$ is the Heaviside function at the corresponding collocation point α. The subtraction of the enrichment function by this term triggers the shifting approach [77]. In this initial proposition, the need for blending elements is avoided. This implies that the Heaviside enrichment on fully cut faces should consider shifted basis functions. Further, for partially cut faces including a crack tip, in Section 2.2, the entire face is enriched with the Williams solution and no shifting is considered. $\phi_{\alpha}^{\gamma\mathscr{H}}$ is the basis function contained in the set of $n_{\mathscr{H}}^{\gamma}$ enriched functions, which is reduced because of the local support of the Heaviside enrichment. Lastly, displacement coefficients $\overline{d}_k^{\beta}$ come as additional unknowns that represent the jump in displacements at the enriched surface.

The introduction of the expanded approximation for u_k^{γ} (Eq. (1)) on the BIEs, by applying the same procedure that obtains the standards IGABEM Displacement BIE (DBIE) and Traction BIE (TBIE), Eq. (A.10), leads to the modified discretised equations as:

$$\begin{aligned} c_{\ell k}(\hat{\mathbf{x}}) \sum_{\alpha=1}^{n^{\gamma}} \phi_{\alpha}^{\hat{\gamma}}(\hat{\mathbf{x}}) d_k^{\beta} + \sum_{\gamma=1}^{NS} \underline{\mathrm{T}}^{*\alpha\gamma}_{\ell k} d_k^{\beta} + \sum_{\gamma=1}^{NS} \underline{\mathrm{T}}_{\mathrm{h}\ell k}^{\alpha\gamma} \overline{d}_k^{\beta} &= \sum_{\gamma=1}^{NS} \underline{\mathrm{U}}^{*\alpha\gamma}_{\ell k} p_k^{\beta} \\ c_{\ell k}(\hat{\mathbf{x}}) \sum_{\alpha=1}^{n^{\gamma}} \phi_{\alpha}^{\hat{\gamma}}(\hat{\mathbf{x}}) p_k^{\beta} + n_{\ell}(\hat{\mathbf{x}}) \sum_{\gamma=1}^{NS} \underline{\mathrm{S}}^{\alpha\gamma}_{k\ell j} d_k^{\beta} + n_{\ell}(\hat{\mathbf{x}}) \sum_{\gamma=1}^{NS} \underline{\mathrm{S}}_{\mathrm{h}k\ell j}^{*\alpha\gamma} \overline{d}_k^{\beta} &= n_{\ell}(\hat{\mathbf{x}}) \sum_{\gamma=1}^{NS} \underline{\mathrm{D}}^{*\alpha\gamma}_{k\ell j} p_k^{\beta} \end{aligned} \tag{2}$$

in which solely $\underline{\mathrm{T_h}}^{\alpha\gamma}_{\ell k}$ and $\underline{\mathrm{S_h}}^{*\alpha\gamma}_{k\ell j}$ emerge from enrichment function influence, being:

$$\begin{aligned}\underline{\mathrm{T_h}}^{\alpha\gamma}_{\ell k} &= \sum_{\mathrm{ks}=1}^{n^{\gamma}_{\mathrm{ks}}}\sum_{\alpha=1}^{n^{\gamma}_{\mathscr{H}}}\int_{\Lambda} T^{*}_{\ell k}\phi^{\gamma\mathscr{H}}_{\alpha}\left(\mathscr{H}-\mathscr{H}_{\alpha}\right) J^{\mathrm{ks}}_{\gamma}\, d\Lambda \\ \underline{\mathrm{S_h}}^{*\alpha\gamma}_{k\ell j} &= \sum_{\mathrm{ks}=1}^{n^{\gamma}_{\mathrm{ks}}}\sum_{\alpha=1}^{n^{\gamma}_{\mathscr{H}}}\int_{\Lambda} S^{*}_{k\ell j}\phi^{\gamma\mathscr{H}}_{\alpha}\left(\mathscr{H}-\mathscr{H}_{\alpha}\right) J^{\mathrm{ks}}_{\gamma}\, d\Lambda\end{aligned} \tag{3}$$

The definition of the enriched basis functions is directly related to the number of added degrees of freedom. The set $\phi^{\gamma\mathscr{H}}_{\alpha}$ consists of all non-null basis functions of each knot-span crossed by the crack. The implementation details associated to this task in the isogeometric context are presented in Section 3.1. A key complication is that the introduction of the unknowns $\overline{d}^{\beta}_{k}$ does not naturally come with additional equations, which leads to an ill-posed system containing an insufficient number of equations. Strategies to obtain the auxiliary equations required for this, and other enrichment strategies of this study, are presented in Section 2.4. Note that all terms arising from a standard IGABEM analysis are still present in the augmented system, highlighting the straightforward introduction of enrichment in pre-existing IGABEM codes.

The shifting procedure removes the requirement for the CPV in the DBIE and for HFP in the TBIE in the SST for the strongly singular and hypersingular integrals. Consequently, the SST for the S^{*} kernel does not require the first derivative of the enrichment function, which constitutes an advantage of this approach compared against the use of unshifted enrichment functions. Additionally, the influence of the Heaviside enrichment on the jump term cancels out as a consequence of the shifting procedure.

Another aspect of the integration of the kernels in Eq. (3) is its discontinuous nature over the crossed knot-span. In this case, as standard for the GFEM/XFEM [25],its accuracy depends on an element subdivision scheme to correctly account for each continuous contribution. More details of the generation of a cell-based subdivision and integration are presented in Sections 3.1 and 3.2.

2.2. Williams solution enrichment for $\sqrt{r}$ behaviour on cut surfaces

Edge cracks present an enormous challenge for boundary-based methods, because of the requirement of aligned meshes between the external boundary and crack surfaces. In addition, the displacements over the crack surface exhibit a classical $\sqrt{r}$ behaviour found in LEFM, with r being the distance from the crack front. Standard NURBS basis functions and the Heaviside enrichment cannot precisely capture this for the external boundary partially cut by the crack, which leads to a sub-optimal convergence. In this context, this study proposes a displacement field enrichment for partially cut surfaces based on the leading order term of the Williams expansion [78]. This expansion leads to the augmented displacement field as:

$$u^{\gamma\mathscr{T}}_{k}(\xi_1,\xi_2) = \sum_{\alpha=1}^{n^{\gamma}}\phi^{\gamma}_{\alpha}(\xi_1,\xi_2)d^{\beta}_{k} + \sum_{\alpha=1}^{n^{\gamma}}\phi^{\gamma}_{\alpha}(\xi_1,\xi_2)R_{kq}\psi^{\gamma}_{qM}\hat{d}^{\beta}_{M} \tag{4}$$

in which the additional unknowns $\hat{d}^{\beta}_{M}$ represent the magnitudes related to the enrichment function ψ^{γ}_{qM}. R_{kq} is a rotation matrix from the local coordinate system at the crack front, where ψ^{γ}_{qM} is defined, to the global coordinate system, according to Fig. 1. The Williams-based enrichment function, ψ^{γ}_{qM}, is:

$$\begin{aligned}\psi_{qM} &= \begin{bmatrix}\psi_{nI} & \psi_{nII} & \psi_{nIII}\\ \psi_{bI} & \psi_{bII} & \psi_{bIII}\\ \psi_{tI} & \psi_{tII} & \psi_{tIII}\end{bmatrix}\\ \psi_{nI} &= \frac{1}{2\mu}\sqrt{\frac{r^{t}}{2\pi}}\cos\left(\frac{\theta^{t}}{2}\right)\left[\kappa-1+2\sin^{2}\left(\frac{\theta^{t}}{2}\right)\right]\\ \psi_{nII} &= \frac{1}{2\mu}\sqrt{\frac{r^{t}}{2\pi}}\sin\left(\frac{\theta^{t}}{2}\right)\left[\kappa+1+2\cos^{2}\left(\frac{\theta^{t}}{2}\right)\right]\\ \psi_{bI} &= \frac{1}{2\mu}\sqrt{\frac{r^{t}}{2\pi}}\sin\left(\frac{\theta^{t}}{2}\right)\left[\kappa+1-2\cos^{2}\left(\frac{\theta^{t}}{2}\right)\right]\\ \psi_{bII} &= -\frac{1}{2\mu}\sqrt{\frac{r^{t}}{2\pi}}\cos\left(\frac{\theta^{t}}{2}\right)\left[\kappa-1-2\sin^{2}\left(\frac{\theta^{t}}{2}\right)\right]\\ \psi_{tIII} &= \frac{1}{2\mu}\sqrt{\frac{r^{t}}{2\pi}}4\sin\left(\frac{\theta^{t}}{2}\right)\\ \psi_{tI} &= \psi_{tII} = \psi_{nIII} = \psi_{bIII} = 0\end{aligned} \tag{5}$$

in which r^{t} is the distance to the crack tip, θ^{t} is the angle between the tangent vector in the local coordinate system and the vector $\mathbf{r^{t}}$, as defined in Appendix C. κ is the Kolosov constant, being $\kappa = 3-4\nu$ for plane-strain and $\kappa = \frac{3-\nu}{1+\nu}$ for plane-stress and $\mu = \frac{E}{2(1+\nu)}$ is the shear modulus. This proposition is similar to the Oden–Duarte [14,79] enrichment, but with the major difference that here all enrichment functions are combined based on the rotation matrix to become a single function multiplying each additional unknown.

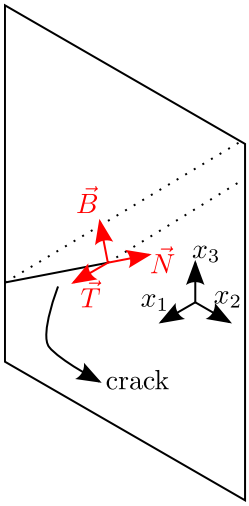

Fig. 1. Local coordinate system at the crossing between crack and external face.

In this study a Williams-based enrichment is applied to all NURBS basis functions on the partially cut surface, which justifies the use of ϕ^{γ}_{α} on both standard and enriched terms of Eq. (4). Then, the substitution of the expanded displacements in Eq. (4) on the BIEs results in a similar equation to that in the standard IGABEM, Eq. (A.10), but with an additional kernel, as:

$$\begin{aligned}
&c_{\ell k}(\hat{\mathbf{x}})\sum_{\alpha=1}^{n^{\gamma}}\phi^{\hat{\gamma}}_{\alpha}(\hat{\mathbf{x}})d^{\beta}_{k}+c_{\ell k}(\hat{\mathbf{x}})\sum_{\alpha=1}^{n^{\gamma}}\phi^{\hat{\gamma}}_{\alpha}(\hat{\mathbf{x}})R_{kq}(\hat{\mathbf{x}})\psi^{\gamma}_{qM}(\hat{\mathbf{x}})\hat{d}^{\beta}_{M}\\
&\quad+\sum_{\gamma=1}^{NS}\underline{\mathrm{T}}^{*\alpha\gamma}_{\ell k}d^{\beta}_{k}+\sum_{\gamma=1}^{NS}\underline{\mathrm{T}}_{\mathrm{t}}{}^{\alpha\gamma}_{\ell k}\hat{d}^{\beta}_{k}=\sum_{\gamma=1}^{NS}\underline{\mathrm{U}}^{*\alpha\gamma}_{\ell k}p^{\beta}_{k}\\
&c_{\ell k}(\hat{\mathbf{x}})\sum_{\alpha=1}^{n^{\gamma}}\phi^{\hat{\gamma}}_{\alpha}(\hat{\mathbf{x}})p^{\beta}_{k}+c_{\ell k}(\hat{\mathbf{x}})\sum_{\alpha=1}^{n^{\gamma}}\phi^{\hat{\gamma}}_{\alpha}(\hat{\mathbf{x}})R_{kq}(\hat{\mathbf{x}})\psi^{\gamma}_{qM}(\hat{\mathbf{x}})\hat{p}^{\beta}_{k}\\
&+n_{\ell}(\hat{\mathbf{x}})\sum_{\gamma=1}^{NS}\underline{\mathrm{S}}^{\alpha\gamma}_{k\ell j}d^{\beta}_{k}+n_{\ell}(\hat{\mathbf{x}})\sum_{\gamma=1}^{NS}\underline{\mathrm{S}}_{\mathrm{t}}{}^{*\alpha\gamma}_{k\ell j}\hat{d}^{\beta}_{k}=n_{\ell}(\hat{\mathbf{x}})\sum_{\gamma=1}^{NS}\underline{\mathrm{D}}^{*\alpha\gamma}_{k\ell j}p^{\beta}_{k}
\end{aligned}\tag{6}$$

in which $\underline{\mathrm{T}}_{\mathrm{t}}{}^{\alpha\gamma}_{\ell k}$ and $\underline{\mathrm{S}}_{\mathrm{t}}{}^{*\alpha\gamma}_{k\ell j}$ are new kernels originated from the Williams-based enrichment, being:

$$\begin{aligned}
\underline{\mathrm{T}}_{\mathrm{t}}{}^{\alpha\gamma}_{\ell k}&=\sum_{\mathrm{ks}=1}^{n^{\gamma}_{\mathrm{ks}}}\sum_{\alpha=1}^{n^{\gamma}}\int_{\Lambda}T^{*}_{\ell k}\phi^{\gamma}_{\alpha}R_{kq}\psi^{\gamma}_{qM}J^{\mathrm{ks}}_{\gamma}\,d\Lambda\\
\underline{\mathrm{S}}_{\mathrm{t}}{}^{*\alpha\gamma}_{k\ell j}&=\sum_{\mathrm{ks}=1}^{n^{\gamma}_{\mathrm{ks}}}\sum_{\alpha=1}^{n^{\gamma}}\int_{\Lambda}S^{*}_{k\ell j}\phi^{\gamma}_{\alpha}R_{kq}\psi^{\gamma}_{qM}J^{\mathrm{ks}}_{\gamma}\,d\Lambda
\end{aligned}\tag{7}$$

Analogously to the Heaviside enrichment (Section 2.1), the Williams-based expansion of the displacements does not change the standard IGABEM coefficients, which are retained in the BEM matrices, while introducing additional parameters to the discretisation. Thus, it shares the capability of being directly incorporated into existing IGABEM computational codes. Additional equations are necessary due to the addition of new unknowns, similarly to the Heaviside enrichment, and this is tackled in Section 2.4. Another similarity comes from the discontinuous nature of the term $\sin\frac{\theta}{2}$, requiring integration over a cell-based subdivision, as detailed in Section 3.1.

In this study, the main focus is the first development of the extended IGABEM for 3D fracture mechanics and the calculation of SIFs from the crack front enrichment depicted in Section 2.3. A simple unshifted Williams enrichment is applied on the partially crossed faces. Since the shifting approach has not been applied for the Williams solution enrichment, singularities arise and they must be treated accordingly by using the SST, as detailed in Appendix B. Then, derivatives of both ψ_{qM} and R_{kq} are required with respect to the parent coordinate space, where integration is carried out. Their expressions are in the Appendix C.

2.3. Crack front enrichment for the direct SIF extraction

The enrichment strategy for the introduction of SIFs as additional unknowns consists of using the Williams-based enrichment function (Eq. (5)) on the crack surfaces. In addition, these parameters are interpolated by uni-directional NURBS basis functions

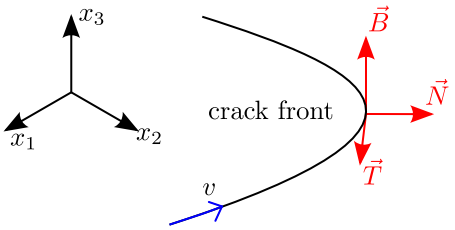

Fig. 2. Local coordinate system for crack front enrichment.

over the crack front, which leads to the following enriched displacement field for the crack surface:

$$u_k^{\gamma^{+/-}}(\xi_1,\xi_2) = \sum_{\alpha=1}^{n^\gamma} \phi_\alpha^{\gamma^{+/-}}(\xi_1,\xi_2) d_k^\beta + \sum_{s=1}^{n_K^\gamma} \tilde{\phi}_s^{\mathrm{cf}}(\upsilon) R_{kq}^{\mathrm{cf}} \psi_{qM}^{\bar{\gamma}^{\mathrm{cf}}} \tilde{K}_M^{s\,\mathrm{cf}} \tag{8}$$

in which $\tilde{\phi}_s^{\mathrm{cf}}(\upsilon)$ is the uni-directional NURBS basis functions over the crack front cf that interpolates the SIFs coefficients $\tilde{K}_M^{s\,\mathrm{cf}}$. This set of basis functions comes from the corresponding univariate NURBS curve in the crack front that generates the crack surface $\gamma^{+/-}$. Thus, each crack front introduces n_K^γ additional unknowns related to the distribution of SIFs along the front. The incorporation of Eq. (8) in the BIEs yields to:

$$\begin{aligned}
&c_{\ell k}(\hat{\mathbf{x}}) \sum_{\alpha=1}^{n^\gamma} \phi_\alpha^{\hat{\gamma}}(\hat{\mathbf{x}}) d_k^\beta + c_{\ell k}(\hat{\mathbf{x}}) \sum_{s=1}^{n_K^\gamma} \tilde{\phi}_s^{\mathrm{cf}}(t(\hat{\mathbf{x}})) R_{kq}^{\mathrm{cf}}(\hat{\mathbf{x}}) \psi_{qM}^{\bar{\gamma}^{\mathrm{cf}}}(\hat{\mathbf{x}}) \tilde{K}_M^{s\,\mathrm{cf}} \\
&\quad + \sum_{\gamma=1}^{NS} \underline{\mathrm{T}}_{\ell k}^{*\alpha\gamma} d_k^\beta + \sum_{\gamma=1}^{NS} \underline{\mathrm{T}}_{\mathrm{s}\,\ell k}^{s\,\mathrm{cf}} \tilde{K}_M^{s\,\mathrm{cf}} = \sum_{\gamma=1}^{NS} \underline{\mathrm{U}}_{\ell k}^{*\alpha\gamma} p_k^\beta \\
&c_{\ell k}(\hat{\mathbf{x}}) \sum_{\alpha=1}^{n^\gamma} \phi_\alpha^{\hat{\gamma}}(\hat{\mathbf{x}}) p_k^\beta + c_{\ell k}(\hat{\mathbf{x}}) \sum_{s=1}^{n_K^\gamma} \tilde{\phi}_s^{\mathrm{cf}}(t(\hat{\mathbf{x}})) R_{kq}^{\mathrm{cf}}(\hat{\mathbf{x}}) \psi_{qM}^{\bar{\gamma}^{\mathrm{cf}}}(\hat{\mathbf{x}}) \tilde{K}_M^{s\,\mathrm{cf}} \\
&+ n_\ell(\hat{\mathbf{x}}) \sum_{\gamma=1}^{NS} \underline{\mathrm{S}}_{k\ell j}^{*\alpha\gamma} d_k^\beta + n_\ell(\hat{\mathbf{x}}) \sum_{\gamma=1}^{NS} \underline{\mathrm{S}}_{\mathrm{s}\,k\ell j}^{s\,\mathrm{cf}} \tilde{K}_M^{s\,\mathrm{cf}} = n_\ell(\hat{\mathbf{x}}) \sum_{\gamma=1}^{NS} \underline{\mathrm{D}}_{k\ell j}^{*\alpha\gamma} p_k^\beta
\end{aligned} \tag{9}$$

in which, analogously to both Heaviside and Williams-based enrichment, a new kernel arises in each BIE as:

$$\begin{aligned}
\underline{\mathrm{T}}_{\mathrm{s}\,\ell k}^{s\,\mathrm{cf}} &= \sum_{\mathrm{ks}=1}^{n_{\mathrm{ks}}^{\gamma(\mathrm{cf})}} \sum_{s=1}^{n_K^\gamma} \int_\Lambda T_{\ell k}^* \tilde{\phi}_s^{\mathrm{cf}} R_{kq}^{\mathrm{cf}} \psi_{qM}^{\gamma(\mathrm{cf})} J_{\gamma(\mathrm{cf})}^{\mathrm{ks}} \, d\Lambda \\
\underline{\mathrm{S}}_{\mathrm{s}\,k\ell j}^{s\,\mathrm{cf}} &= \sum_{\mathrm{ks}=1}^{n_{\mathrm{ks}}^{\gamma(\mathrm{cf})}} \sum_{s=1}^{n_K^\gamma} \int_\Lambda S_{k\ell j}^* \tilde{\phi}_s^{\mathrm{cf}} R_{kq}^{\mathrm{cf}} \psi_{qM}^{\gamma(\mathrm{cf})} J_{\gamma(\mathrm{cf})}^{\mathrm{ks}} \, d\Lambda
\end{aligned} \tag{10}$$

This integration takes place at the enriched crack surface. The kernels make use of the uni-directional coordinate t for the crack front projection at each Gauss point, which is obtained by a point projection algorithm [80].

Special care must be taken in the rotation matrix definition. For a crack front, Fig. 2 defines the local coordinate system of the Williams solution, which may change depending on the crack geometry. The present research applies the Frenet–Serret frame [81,82] to accurately determine both the rotation matrix and its derivatives based on the crack front NURBS parametrisation, as shown in Appendix C. For flat cracks, the rotation matrix is simplified by having $\vec{T}$ parallel to the crack front, $\vec{N}$ aligned to the normal outward vector of the upper crack surface (over which we apply the DBIE), with $\vec{B} = \vec{T} \times \vec{N}$.

Besides allowing a direct determination of the SIFs, and thereby precluding post-processing tasks, this strategy also introduces the $\sqrt{r}$ behaviour in the formulation, giving rise to accuracy improvements. The enrichment is applied over the entire crack surface, instead of solely at the portion closest to the crack front. Extending the enrichment over the whole crack surface gives rise to no additional degrees of freedom. To accommodate the new unknowns that are proxies for the SIFs, Section 2.4 presents a specific scheme to generate auxiliary equations using crack front tying to enforce displacement continuity at the crack front. This results in the SIFs becoming available in the solution vector as terms $\tilde{K}_M^{s\,\mathrm{cf}}$.

The SIF determination occurs in a straightforward manner by simple interpolation at the crack front from the obtained unknowns $\tilde{K}_M^{s\,\mathrm{cf}}$. In this matter, it is worth mentioning the differences between the approach herein and the special crack tip element successfully proposed by Li, Mear and Xiao [83] in the Symmetric Galerkin BEM approach. Their study proposed a different set of basis functions containing the $\sqrt{r}$ behaviour for the crack front elements, which culminates in a change in the construction of the H and G influence matrices. On the other hand, the present study allows the direct introduction of the SIF parameters without changes in the existing H and G matrices from IGABEM.

2.4. Additional equations and XIGABEM algebraic system

The use of enrichment functions in addition to the standard NURBS basis functions introduces new unknowns. Unlike Galerkin-based schemes, this becomes challenging in a collocation-based IGABEM formulation because collocating only at the existing collocation points will produce an insufficient number of equations given the increased number of unknowns. In this study, the additional equations for the three-dimensional XIGABEM come from two different procedures: one for both Heaviside and Williams-based enrichment and another one for the crack front enrichment that directly contains the SIFs.

The strategy associated with the Heaviside and Williams-based enrichment functions applies the TBIE on the collocation points whose basis functions are enriched (in addition to the DBIE already used). Then, these collocation points receive simultaneously DBIE and TBIE, and, due to the linear independence nature of these two integral representations, the resulting equations are not redundant. A feasible alternative strategy might be additional collocation points [44], but the TBIE approach dismisses the requirement to determine a suitable location for additional collocation points.

Remark. The SST of the TBIE requires Hölder continuity at the collocation point, in which the first derivative of the displacement field (for the S^* kernel) must be C^1 continuous at the singular point. However, for degree 1 NURBS surfaces, the Greville Abscissae scheme locates these points where the basis functions are C_0. Then, the sole application of the SST is not sufficient for the accurate evaluation of the hypersingular integrals. To overcome this issue, the rigid body motion approach [84] is a useful alternative to compute the missing contribution. This strategy considers a body under no traction in its boundary, which leads to a constant displacement u_k^{RBM} field in the body. Additionally, once the parameters introduced by the extended IGABEM are associated to crack opening and to the asymptotic behaviour at the crack, they do not exist in a rigid body motion context, hence being zero. In this context, the TBIE becomes:

$$\left(n_\ell(\hat{\mathbf{x}})\sum_{\gamma=1}^{NS}\underline{\mathrm{S}}_{k\ell j}^{*\alpha\gamma}\right)u_k^{\mathrm{RBM}}=0_k \tag{11}$$

Considering that Eq. (11) holds for any arbitrary u_k^{RBM}, the terms inside the parentheses must be zero. Therefore, it is possible to find the missing terms that must be spread over the contributions associated to the S^* kernel as:

$$\begin{aligned}&\left(-n_\ell(\hat{\mathbf{x}})\sum_{\gamma=1}^{NS}\underline{\mathrm{S}}_{k\ell j}^{*\alpha\gamma}\right)\sum_{\alpha=1}^{n^\gamma}\phi_\alpha^{\hat{\gamma}}(\hat{\mathbf{x}})d_k^\beta+c_{\ell k}(\hat{\mathbf{x}})\sum_{\alpha=1}^{n^\gamma}\phi_\alpha^{\hat{\gamma}}(\hat{\mathbf{x}})p_k^\beta\\&+n_\ell(\hat{\mathbf{x}})\sum_{\gamma=1}^{NS}\mathrm{S}_{k\ell j}^{\alpha\gamma}d_k^\beta+n_\ell(\hat{\mathbf{x}})\sum_{\gamma=1}^{NS}\underline{\mathrm{S}}_{\mathrm{h}k\ell j}^{*\alpha\gamma}\overline{d}_k^\beta=n_\ell(\hat{\mathbf{x}})\sum_{\gamma=1}^{NS}\underline{\mathrm{D}}_{k\ell j}^{*\alpha\gamma}p_k^\beta\end{aligned} \tag{12}$$

which must be applied specifically for $p=1$ or $q=1$ NURBS patches in the XIGABEM scheme. The algebraic system receives this correction term after the integration of the boundary, in which Eq. (11) determines its corresponding sum.

For the direct SIF enrichment scheme applied on the crack surfaces, the additional equations are obtained by considering compatibility at the crack front. Both upper and lower crack faces are expected to experience identical displacement at the crack front. However, the discontinuous BEM approach for fracture mechanics cannot guarantee this behaviour. In two-dimensional analysis, it has been shown that a 'tying equation' enforcing displacement continuity at a crack tip is a simple approach to provide an additional equation, but it is also advantageous in that the unknowns $\tilde{K}_M^{s\,\mathrm{cf}}$ from Eq. (8) become good approximations to the SIFs [46,48]. In the three-dimensional scope that is the focus of the current work, the crack front is a curve, and a weak-form strategy is presented to enforce compatibility as:

$$\int_{\Gamma_s^{\mathrm{cf}}}\left[\phi_\alpha^{\bar{\gamma}^+}(\xi_1,\xi_2)d_k^{\beta+}-\phi_\alpha^{\bar{\gamma}^-}(\xi_1,\xi_2)d_k^{\beta-}\right]\tilde{\phi}_s^{\mathrm{cf}}(v)dv=0_k \tag{13}$$

in which Γ_s^{cf} is the line describing the crack front. $\tilde{\phi}_s^{\mathrm{cf}}$ is the weighting function chosen for this weak-form compatibility; here we adopt the NURBS function that interpolates the SIFs.

The final extended IGABEM algebraic system assumes its form by augmenting the standard IGABEM algebraic matrix, Eq. (A.15) with the effects of the enrichment functions on the BIEs, which are Eq. (2), Eq. (6) and Eq. (9). By introducing also the additional equations as described, the XIGABEM system becomes:

$$\begin{bmatrix}\mathbf{H}&\mathbf{H}_{\mathrm{h}}&\mathbf{H}_{\mathrm{t}}&\mathbf{H}_{\mathrm{s}}\\\mathbf{H}^{\mathrm{T}}&\mathbf{H}_{\mathrm{h}}^{\mathrm{T}}&\mathbf{H}_{\mathrm{t}}^{\mathrm{T}}&\mathbf{H}_{\mathrm{s}}^{\mathrm{T}}\\\boldsymbol{\Phi}_{\mathrm{s}}&\mathbf{0}&\mathbf{0}&\mathbf{0}\end{bmatrix}\begin{Bmatrix}\mathbf{d}\\\overline{\mathbf{d}}\\\hat{\mathbf{d}}\\\tilde{\mathbf{K}}\end{Bmatrix}=\begin{bmatrix}\mathbf{G}\\\mathbf{G}^{\mathrm{T}}\\\mathbf{0}\end{bmatrix}\{\ \mathbf{p}\ \} \tag{14}$$

in which $\mathbf{H}$, $\mathbf{G}$, $\mathbf{d}$ and $\mathbf{p}$ refer to the standard IGABEM contributions. The subscript h refers to the contribution from the Heaviside enrichment for fully cut faces in the external boundary, Eq. (2). In addition, the terms with the subscript t contain the results from the Williams-based enrichment for partially cut faces, coming from Eq. (6). The subscript s stands for the crack front enrichment contributions, Eq. (8). The superscript T indicates the TBIE coefficients when applied at the collocation points whose basis functions are enriched. $\boldsymbol{\Phi}_{\mathrm{s}}$ is the sub-matrix containing the contributions from Eq. (13). Lastly, $\overline{\mathbf{d}}$, $\hat{\mathbf{d}}$ and $\tilde{\mathbf{K}}$ are the additional unknowns from the Heaviside, Williams-based and crack front enrichment strategies, respectively. By applying the boundary conditions on Eq. (14)

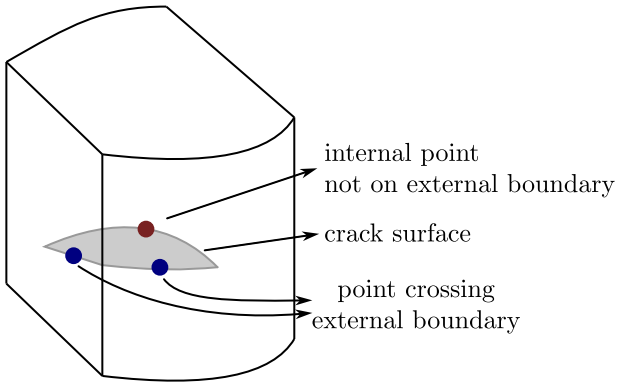

Fig. 3. Mid-points at each crack edge that search their correspondent external boundary face.

in the same manner as for the standard IGABEM, a linear system $\mathbf{Ax} = \mathbf{b}$ is obtained, and use of a standard solver recovers all standard displacement and traction parameters in the solution vector $\mathbf{x}$, as well as the unknowns associated with the enrichment functions.

3. Implementation aspects

3.1. Crossing detection between crack face and cut face

The detection of the crossings between the crack faces and the external boundary is fundamental to the extended IGABEM, as it allows the crack surface geometry to be fully defined and completes the definition of the enriched basis functions. It also provides important geometric information on the crossed NURBS patch. This task consists of searching the external boundary NURBS surfaces that contain the mid-point of each upper crack face edge (those with the DBIE applied), as depicted in Fig. 3. This search algorithm makes use of a Newton–Raphson method to find the associated parametric coordinates that give the geometric coordinates of each mid-point. Then, each NURBS surface found is then classified as enriched, in which either the Heaviside or the Williams-based functions will be applied, the choice depending on whether the face is fully or partially cut. Similarly, a search for the corresponding lower crack face edge takes place to define the pair of crack face edges that account for the enrichment.

The next step is to project the crack edge on the enriched NURBS surface. Then, the intersecting NURBS curve on the crossed surface has the same degree, knot-span and number of control points as the univariate NURBS curve that generates the upper crack face and crosses the external boundary, as in Fig. 3. The objective is to generate a NURBS curve for the crack edge in the parametric space of the enriched NURBS surface, so that further geometric procedures will be taken directly on the external boundary NURBS parametric space. To find the corresponding control points in the parametric space, a sample of t_s anchor points on the crossing crack edge are first defined, based on the Greville Abscissae. For each anchor point, the NURBS basis functions are computed, and also the parametric coordinates in the projected NURBS surface, which results in the following algebraic system:

$$\begin{aligned} \sum_{k=1}^{n} \phi^k(t_s)\xi_1^s &= \xi_1(t_s) \\ \sum_{k=1}^{n} \phi^k(t_s)\xi_2^s &= \xi_2(t_s) \end{aligned} \tag{15}$$

in which the pair (ξ_1^s, ξ_2^s) refers to the control points written in the parametric coordinates of the enriched patch, and the pair $\big(\xi_1(t_s), \xi_2(t_s)\big)$ refers to the parametric coordinate on the enriched patch that returns the same geometric position in the physical space as t_s from the NURBS curve. Lastly, $\phi^k(t_s)$ is the basis function value. In this procedure, each new control point inherits its weight from that of the corresponding control point from the univariate edge NURBS curve.

Additionally, it is helpful to detect the intersection between the projected NURBS curve and the knot-span limits at the enriched patch. These points are further needed to define the sub-cells for integration, as well as to classify the face as fully or partially cut, and to define the enriched basis functions for the Heaviside enrichment. This detection consists of a marching through the parametric coordinate of the projected NURBS curve in incremental steps of $\delta = (t_L - t_F)/n_s$, in which t_F and t_L are the first and last knots, and n_s is the number of divisions. For each $t_i = t_F + i\delta$, the obtaining of the pair $\big(\xi_1(t_i), \xi_2(t_i)\big)$ allows the detection of its corresponding knot-span in each univariate direction. When there is a change in the knot-span from t_{i+1} compared against t_i in the direction dir, a crossing occurs for a NURBS curve parametric coordinate t_c such as $t_i \leq t_c \leq t_{i+1}$. Then, a local Newton–Raphson procedure determines t_c, in which the associated residual is $E(t) = \xi_{\text{dir}}^S - \xi_{\text{dir}}(t)$, where ξ_{dir}^S is the known parametric coordinate at the external boundary surface. By expanding $E(t)$ in its first term of Taylor Series, the increment δt_k is:

$$\Delta t_k = \frac{E(t_k)}{\left.\frac{\partial E}{\partial t}\right|_k} \tag{16}$$

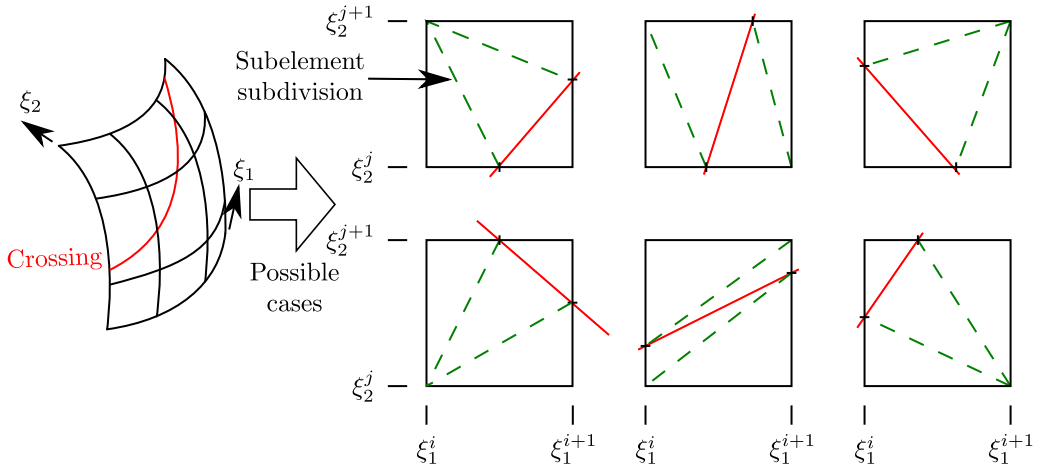

Fig. 4. Possible cases for entirely crossed knot-span, in which the crack is indicated by red and the knot-span sub-divisions are represented in dashed green.

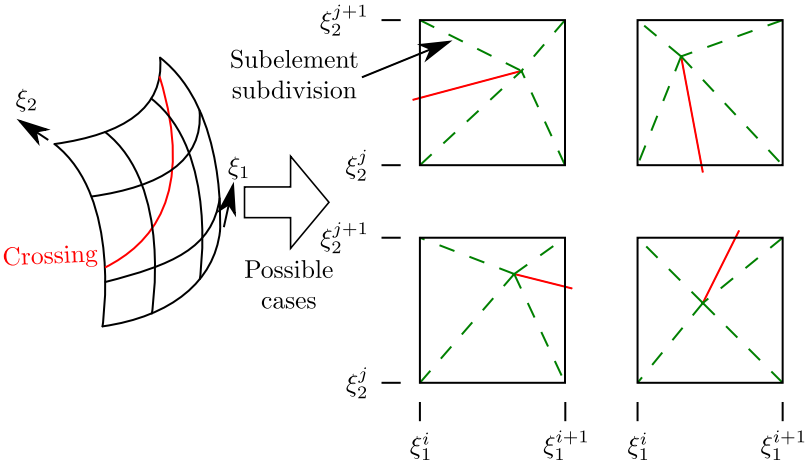

Fig. 5. Knot-span subdivision for crack ending inside its domains.

in which there is an update as $t_{k+1} = t_k + \Delta t_k$ until the residual is smaller than a given tolerance. The derivative $\partial E/\partial t$ is the tangent vector component in the dir direction.

If one of the ends of the NURBS curve that represents the crack lies inside the enriched surface, this patch can be defined as partially cut, and all basis functions on the patch will be enriched by the Williams-based enrichment function. On the other hand, when both ends of the NURBS curve cross the NURBS surface edges, it is a fully cut face. For this fully cut patch, all non-null basis functions at $\left(\xi_1(t_c^k), \xi_2(t_c^k)\right)$, in which $t_c^k = (t_c^{k+1} + t_c^k)/2$, are enriched by the Heaviside function. This represents the influence zone required for the Heaviside enrichment at the crossing, once t_c^k lies exactly on the crack.

The numerical integration of the kernels arising from the enrichment strategy demands a sub-cell approach to account separately for the contribution of each term due to the discontinuous nature of the enrichment functions. Therefore, the intersection between the NURBS curve that represents the crack and each knot-span allows the generation of sub-cells, over which Gauss–Legendre integration can safely be applied independently. There are six possible cases for the generation of the sub-cells in entirely crossed knot-spans, which are shown in Fig. 4. In addition, when the crack ends inside a knot-span there are four possible sub-cell configurations, illustrated by Fig. 5.

Since the Heaviside function $\mathscr{H}$ takes a constant value over each sub-cell, it only needs to be computed once for the cell and do not require assessment separately at each Gauss point, accelerating the integration procedure for the associated enriched kernel. The value of $\mathscr{H}$ can be easily computed as the dot product sign between the vector that goes from one of the crack ends pointing to the interior of the sub-cell (Fig. 6) and the normal outward vector of the upper crack face. The obtaining of $\mathscr{H}_\alpha$ for each collocation point proceeds analogously, by defining the vector from one of the crack ends to the collocation point.

In the context of the integration requiring the SST, the sub-cells of the same knot-span that share the same $\mathscr{H}$ are merged. This allows the use of the SST parameters on the whole face, and also reduces loss of accuracy that could be caused by nearly singular integration of these parts.

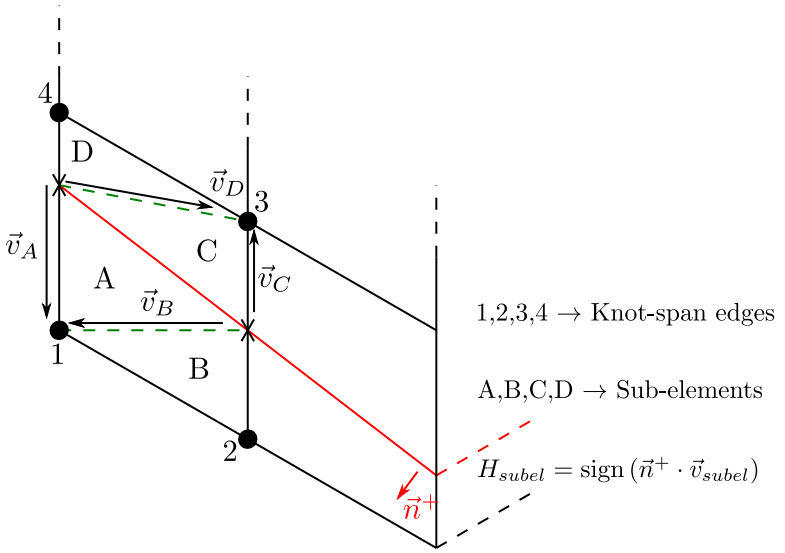

Fig. 6. Heaviside function determination based on dot product between upper surface normal outward vector and internal vector. In this scheme, sub-cells A and B receive $H = +1.0$ while cells C and D have $H = -1.0$.

3.2. Numerical integration of sub-cells

The sub-cell integration requires a specific treatment due to the triangular shape of the cells adopted. Moreover, some cells have the crack curve as one of its edges, which must be accounted for in this process. In this context, this study proposes a polar transformation to perform this task. Three additional mappings are used for relating the NURBS parametric space to the integration space where the Gauss quadrature is performed. This procedure also holds for the singular integration, in which the polar transformation is intrinsically part of the SST.

This strategy starts by defining a pole in which the polar parameters ρ and θ are defined. In the non-singular integration, the pole is at the farthest vertex to the crack curve, while in the singular integration the pole is the collocation point.

The first mapping relates a point from the Gaussian space $\{\hat{\xi}_1, \hat{\xi}_2\} \in \Lambda \,|\, \Lambda = \{[-1;1] \times [-1;1]\}$ to the first auxiliary space $\Omega_1^P = \{[t_1, t_2] \times [0, \hat{\rho}]\}$ as:

$$\begin{aligned} &\mathbf{T}_1^P : (\hat{\xi}_1, \hat{\xi}_2) \rightarrow (t, \rho) \\ &t = \frac{(t_2 - t_1)\hat{\xi}_2}{2} + \frac{(t_2 + t_1)}{2} \\ &\rho = \frac{\hat{\rho}(t)\hat{\xi}_1}{2} + \frac{\hat{\rho}(t)}{2} \end{aligned} \tag{17}$$

in which t refers to the parametric coordinate on the NURBS curve that defines the crack crossing, t_1 and t_2 are the corresponding ends for this coordinate at the sub-cell, and $\hat{\rho}(t)$ is the distance between the pole and the point given by t at the NURBS curve. All these variables are illustrated in Fig. 7. Also, $\hat{\rho}(t)$ expression is:

$$\hat{\rho}(t) = \sqrt{\left[\xi_1(t) - \xi_1^0\right]^2 + \left[\xi_2(t) - \xi_2^0\right]^2} \tag{18}$$

in which (ξ_1^0, ξ_2^0) is the parametric coordinates of the pole in the patch.

The second transformation $\mathbf{T}_2^P$ consists of defining the polar coordinate θ in terms of $(\xi_1(t), \xi_2(t))$ as:

$$\begin{aligned} &\mathbf{T}_2^P : (t, \rho) \rightarrow (\theta, \rho) \\ &\cos\theta = \frac{\xi_1(t) - \xi_1^0}{\hat{\rho}(t)} \\ &\sin\theta = \frac{\xi_2(t) - \xi_2^0}{\hat{\rho}(t)} \\ &\theta = \arctan\left(\frac{\xi_2(t) - \xi_2^0}{\xi_1(t) - \xi_1^0}\right) \end{aligned} \tag{19}$$

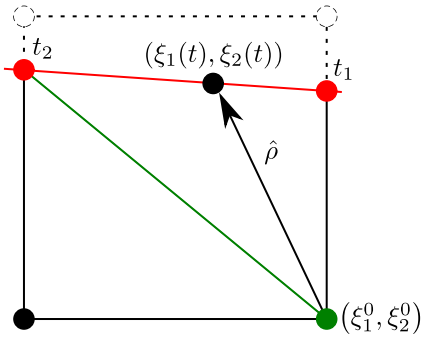

Fig. 7. Variables in $\mathbf{T}_1^P$ mapping.

Lastly, $\mathbf{T}_3^P$ is the transformation that obtains the parametric coordinates pair (ξ_1, ξ_2) at the patch from the polar parameters ρ and θ, as:

$$\begin{aligned} &\mathbf{T}_3^P : (\theta, \rho) \rightarrow (\xi_1, \xi_2) \\ &\xi_1(\rho, \theta) = \xi_1^0 + \rho \cos\theta \\ &\xi_2(\rho, \theta) = \xi_2^0 + \rho \sin\theta \end{aligned} \tag{20}$$

The Jacobian of each transformation enables the integration in the Gauss space going from the NURBS parametric space, and they are:

$$\begin{aligned} \bar{J}_1^{P\gamma} &= \frac{\hat{\rho}(t)}{2} \frac{(t_2 - t_1)}{2} \\ \bar{J}_2^{P\gamma} &= \frac{\mathrm{d}\theta}{\mathrm{d}t} \\ \bar{J}_3^{P\gamma} &= \rho \end{aligned} \tag{21}$$

and the total $d\Gamma_\gamma$ becomes:

$$\begin{aligned} d\Gamma_\gamma &= \left\| \frac{\partial \mathbf{r}}{\partial \hat{\xi}_1} \times \frac{\partial \mathbf{r}}{\partial \hat{\xi}_2} \right\| d\Lambda \\ d\Gamma_\gamma &= \bar{J}_1^{P\gamma} \bar{J}_2^{P\gamma} \bar{J}_3^{P\gamma} J_2^\gamma d\Lambda \end{aligned} \tag{22}$$

in which $\bar{J}_2^{P\gamma}$ comes from the chain rule as:

$$\frac{\mathrm{d}\theta}{\mathrm{d}t} = \frac{\partial\theta}{\partial\xi_1}\frac{\partial\xi_1}{\partial t} + \frac{\partial\theta}{\partial\xi_2}\frac{\partial\xi_2}{\partial t} \tag{23}$$

in which $\partial\xi_1/\partial t$ and $\partial\xi_2/\partial t$ are the components of the NURBS curve tangent vector, and the derivatives in respect to θ are:

$$\begin{aligned} \frac{\partial\theta}{\partial\xi_1} &= \frac{-1}{1 + \left[\dfrac{\xi_2(t) - \xi_2^0}{\xi(t) - \xi_1^0}\right]^2} \frac{\xi_2(t) - \xi_2^0}{\left[\xi_1(t) - \xi_1^0\right]^2} = \frac{\xi_2^0 - \xi_2(t)}{\left[\xi_1(t) - \xi_1^0\right]^2 + \left[\xi_2(t) - \xi_2^0\right]^2} \Rightarrow \\ \frac{\partial\theta}{\partial\xi_1} &= \frac{\xi_2^0 - \xi_2(t)}{\hat{\rho}(t)^2} = \frac{-\sin\theta}{\hat{\rho}(t)} \\ \frac{\partial\theta}{\partial\xi_2} &= \frac{1}{1 + \left[\dfrac{\xi_2(t) - \xi_2^0}{\xi_1(t) - \xi_1^0}\right]^2} \frac{1}{\xi(t) - \xi^0} = \frac{\xi(t) - \xi_1^0}{\left[\xi_1(t) - \xi_1^0\right]^2 + \left[\xi_2(t) - \xi_2^0\right]^2} \Rightarrow \\ \frac{\partial\theta}{\partial\xi_2} &= \frac{\xi_1(t) - \xi_1^0}{\hat{\rho}(t)^2} = \frac{\cos\theta}{\hat{\rho}(t)} \end{aligned} \tag{24}$$

We remark that this scheme holds for triangles which do not have a NURBS curve as one of the edges. In this case, this edge parametrisation consists of a straight line between each edge of the opposite side, and also $t_1 = 0.0$ and $t_2 = 1.0$.

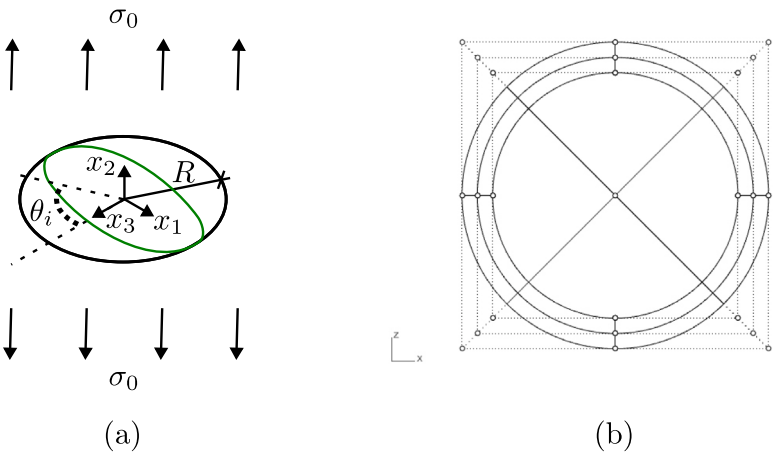

Fig. 8. (a) Geometry and loading conditions for penny-shaped crack and (b) Control points position for penny-shaped crack mesh.

4. Numerical applications

4.1. Penny-shaped crack

The first application of this study is a penny-shaped circular crack with radius $R = 1.0$ embedded in an infinite domain, subjected to a remote uniaxial stress $\sigma_0 = 1.0$, according to Fig. 8(a). Since the Dual BEM formulation herein applied requires the discretisation of the external boundary, the crack is located inside a cube of side $200R$. The material properties are $E = 1.0$ and $\nu = 0.0$. It is noteworthy that the proper choice of the local coordinate system performs a major role for the crack front enrichment scheme when its front is curved. Thus, this application allows the evaluation of the Frenet–Serret frame, especially for mixed mode I/II/III problems. In addition, the analysis of both in-plane and inclined cracks allows the evaluation of a pure mode I and a mixed mode I/II/III in a problem whose enrichment function does not match with the analytical solution. For the pure mode I problem, both SIFs and the u_2 displacement at the crack have a reference solution [85] as:

$$\begin{aligned} u_2(x_1, x_2, x_3) &= \frac{-2n_2(1-\nu)\sigma_0}{\pi\mu}\sqrt{R^2 - (x_1^2 + x_3^2)} \\ K_I &= \frac{2\sigma_0}{\pi}\sqrt{\pi R} \\ K_{II} &= K_{III} = 0 \end{aligned} \tag{25}$$

in which σ_0 is the remote traction applied. For the crack inclined through an angle θ_i, the corresponding SIFs are:

$$\begin{aligned} K_I &= \frac{2\sigma_0}{\pi}\sqrt{\pi R}\cos^2\theta_c \\ K_{II} &= \frac{4\sigma_0}{\pi(2-\nu)}\sqrt{\pi R}\cos\theta_i \sin\theta_i \cos\theta_c \\ K_{III} &= \frac{4\sigma_0(1-\nu)}{\pi(2-\nu)}\sqrt{\pi R}\cos\theta_i \sin\theta_i \sin\theta_c \end{aligned} \tag{26}$$

in which θ_c is the angle of the crack front position taken in the crack plane.

The discretisation adopted for this application consists of an external boundary composed of 6 NURBS surfaces with degree $p = q = 1$ Constant boundary conditions are responsible for representing the uniform stress state in the far field, in which the bottom face ($x_2 = -100.0$) has nil displacements in all directions and there is a traction $t_2 = 1.0$ applied over the top face ($x_2 = 100.0$). For the crack faces, five $p = q = 2$ degree NURBS surfaces describe each face, as illustrated in Fig. 8(b). Each of the four patches that compose the circular crown receive the crack front enrichment, while the central circle remains with only the NURBS basis functions. The circular crown length is set as $R/5$, based on the analysis performed with the Displacement Fitting Technique [73], and the crack front increment chosen by Peng et al. [72] in their penny-shaped crack growth analysis. In addition, a Lagrangian BEM analysis considers a 9-node quadrilateral quadratic element to compare the XIGABEM and IGABEM results against the conventional BEM.

The in-plane crack deformed shape presented in Fig. 9 compares the responses from the extended IGABEM approach and the standard IGABEM for the most refined mesh. A jump in the displacement field at the crack front is evident in the standard formulation, in contrast to the XIGABEM results. For the standard formulation, as previously obtained by Peng et al. [72], the major contribution for the error is at the crack front. The absence of a displacement jump in the XIGABEM solution is a direct consequence of the tying equations.

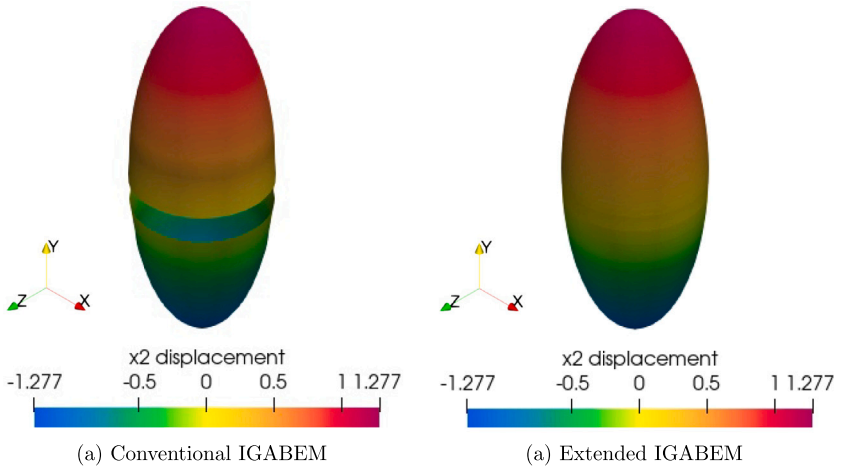

Fig. 9. Deformed shape for penny shaped crack using (a) conventional IGABEM and (b) extended IGABEM.

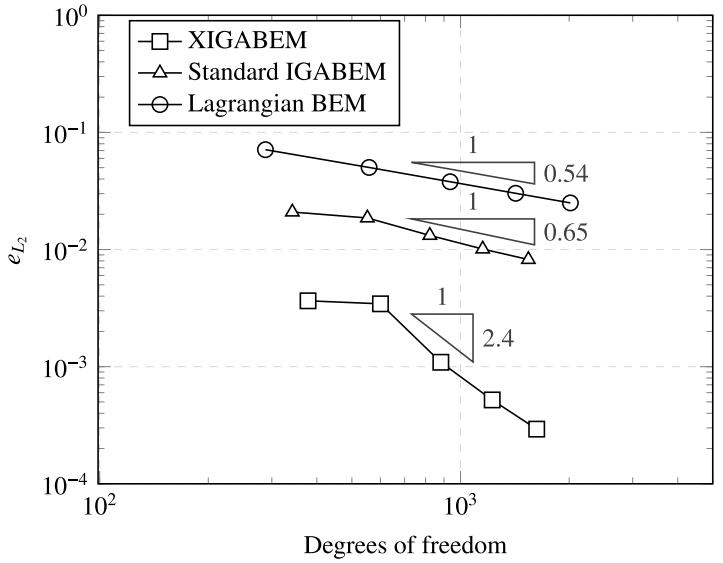

Fig. 10. L_2 norm of error in displacements for in-plane penny-shaped crack.

The convergence analysis in the L_2 norm of error presented in Fig. 10 demonstrates the improvements in the convergence rate for the XIGABEM responses against the standard IGABEM and the Lagrangian BEM. By adding a small number of degrees of freedom, in addition to directly returning the SIFs, there is both a reduction in the L_2 norm of error and an increase in the convergence rate. These outcomes are associated to the asymptotic behaviour introduced by the enrichment, as well as the tying at the crack front. Optimal convergence for collocation methods in the BEM context still has open questions [86,87], but for a smooth problem, Marussig et al. [87] achieved convergence rates of $\mathcal{O}(N^{-p})$ in the L_2 norm, with N being the number of degrees of freedom. For fracture mechanics, this behaviour does not hold, as can be seen in Peng at al [72] and the standard IGABEM simulations used for comparison in Fig. 10 of the present study. On the other hand the XIGABEM approach described herein delivers improved convergence rates over standard IGABEM, both for smooth solutions [87] and for fracture problems.

As widely presented in the literature for the GFEM/XFEM, enrichment strategies can cause an increase in the condition number, which has the potential to become problematic for the system solution. Based on the condition number growth shown in Fig. 11, it is noteworthy that the extended IGABEM formulation for the crack front enrichment improves the overall conditioning when compared against its standard version, instead of worsening it.

Table 1 shows the average relative error for all SIFs to be in excellent agreement with the reference solution, being below 5.10^{-3} for K_1. Additionally, K_2 and K_3 are below 4.10^{-10} for all meshes except the most refined one, in which the effect of near-singular integrals on the evaluation of the BIEs kernels start to influence the overall precision. These results can be improved by an enhanced integration scheme for those integrals, but this is beyond the scope of the present research.

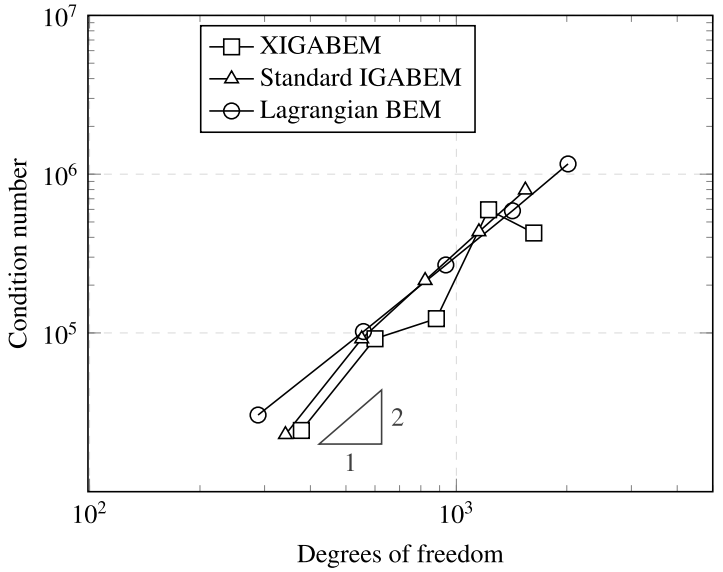

Fig. 11. Condition number growth for in-plane penny-shaped crack.

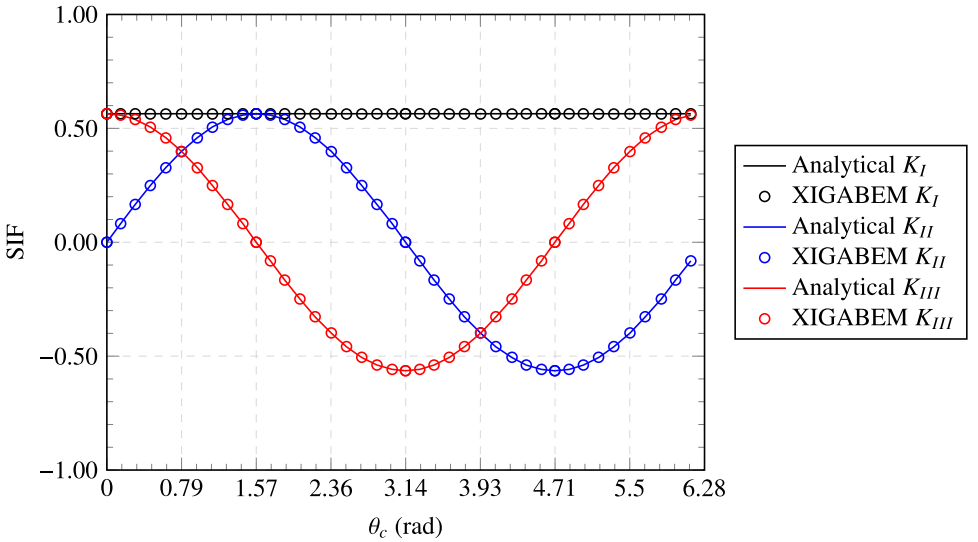

Fig. 12. Stress intensity factors for penny-shaped crack inclined by $\pi/4$ rad.

Table 1
Average SIFs error for in-plane penny-shaped crack.

Degrees of freedom	avg. error in K_1	avg. error in K_2	avg. error in K_3
378	4.689e−03	−2.47e−11	−3.00e−13
600	2.936e−03	−4.11e−11	3.67e−12
882	2.267e−03	3.85e−10	−1.59e−12
1224	1.776e−03	−5.09e−12	4.59e−11
1626	1.432e−03	4.04e−07	−1.22e−11

The numerical analysis for an inclined penny-shaped crack permits the proposed formulation accuracy assessment in the mixed-mode context. For $\theta_i = \pi/4$, Fig. 12 shows the SIFs for the most refined mesh. It is noticed that all SIFs vary in agreement with the reference solutions, with relative errors below 2.03e − 3. Additionally, the L_2 norm of error converges in a faster rate than the SIFs, mainly associated to the correction of the non-physical displacements at the crack front given by the IGABEM formulation. In

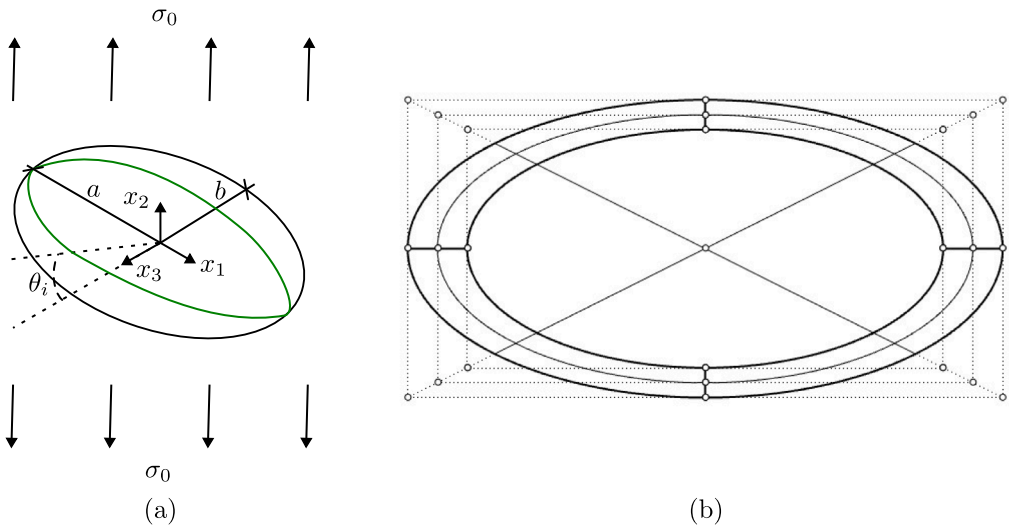

Fig. 13. (a) Geometry of elliptical crack and (b) Mesh and control points for in-plane elliptical mesh.

summary, it is evident that the XIGABEM formulation for a circular crack obtains highly accurate results with an increase of only a few degrees of freedom in comparison to standard approach.

4.2. Elliptical crack

An elliptical crack embedded in an infinite domain and subjected to a far-field uniaxial stress $\sigma_0 = 1.0$ is the second application considered. The crack has semi-major and semi-minor axis dimensions $a = 10.0$ and $b = 5.0$, respectively, as depicted in Fig. 13(a). Similarly to Section 4.1, the truncated domain that represents an infinite medium is a cube with side $200a$. In this application, the mechanical properties are $E = 1.0$ and $\nu = 0.3$. Besides encompassing all the characteristics of Section 4.1 in respect to the definition of the local coordinate system, K_1 is no longer constant, which constitutes an important behaviour to capture by the enrichment scheme. The analytical solution for this case, which also considers the inclination angle θ_i, is [85]:

$$
\begin{aligned}
K_I &= \frac{\sigma_0}{2}(1+2\cos 2\theta_i)\frac{\sqrt{b\pi}f(\theta_c)}{E(k)} \\
K_{II} &= \frac{\sigma_0}{2}(\sin 2\theta_i)\frac{\sqrt{b\pi}k^2 b/a\cos\theta_c}{f(\theta_c)B(k)} \\
K_{III} &= \frac{\sigma_0}{2}(\sin 2\theta_i)\frac{\sqrt{b\pi}k^2(1-\nu)\sin\theta_c}{f(\theta_c)B(k)} \\
k^2 &= 1-\left(\frac{b}{a}\right)^2 \\
f(\theta_c) &= \left[\sin^2\theta_c + \left(\frac{b}{a}\right)^2\cos^2\theta_c\right]^{1/4} \\
B(k) &= (k^2-\nu)E(k) + \nu\left(\frac{b}{a}\right)^2 K(k) \\
K(k) &= \int_0^{\pi/2}\frac{1}{\sqrt{1-k^2\sin^2\theta_c}}d\theta_c \\
E(k) &= \int_0^{\pi/2}\sqrt{1-k^2\sin^2\theta_c}\,d\theta_c
\end{aligned}
\tag{27}
$$

in which $\theta_i = 0$ for an in-plane situation. Particularly, for the in-plane case, the u_2 displacements are:

$$
u_2(x_1, 0, x_3) = \frac{2(1-\nu)\sigma_0}{\mu}\frac{b}{E(k)}\sqrt{1-\frac{x_1^2}{a^2}-\frac{x_3^2}{b^2}} \tag{28}
$$

The crack mesh consists of 5 bi-quadratic NURBS surfaces for each face, in which the internal ellipse is scaled by 80% from the total crack size, as shown in Fig. 13(b). In addition, the external boundary mesh has 6 bi-linear NURBS surfaces. For the convergence study, a knot-insertion strategy is used to increase uniformly in each parametric direction the number of basis functions only at the crack surfaces.

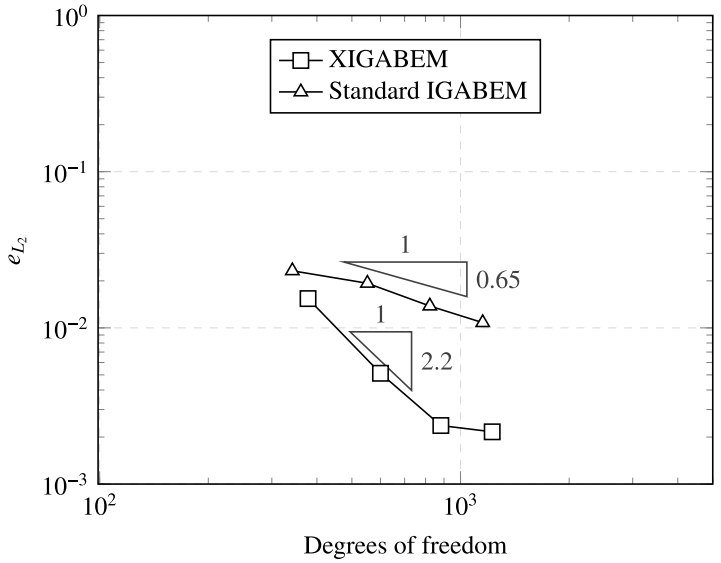

Fig. 14. L_2 norm of error in displacements for in-plane elliptical crack.

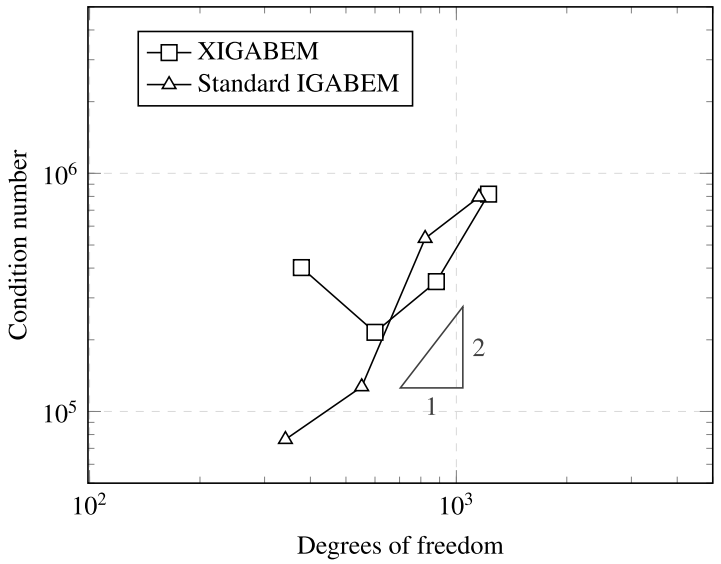

Fig. 15. Condition number growth for in-plane elliptical crack.

The convergence analysis in Fig. 14 demonstrates again an increase in the order of convergence rate for the XIGABEM in comparison to the standard formulation. However, for the most refined mesh, the near-singular integral precision starts to have a mild effect on the solution accuracy. In addition, Fig. 15 shows that the condition number remains similar to the standard formulation. Moreover, the SIFs directly obtained as degrees of freedom, presented in Fig. 16, are in accordance with the analytical solutions for the in-plane case. Thus, the enrichment scheme is also capable of capturing the trigonometrical variation for all three SIFs of this application.

The elliptical crack inclined through angle $\theta_i = \pi/6$ permits an analysis of a complex crack geometry in a mixed-mode loading case. The extracted SIFs are depicted in Fig. 17, in which again the formulation precisely captures the expected behaviour for all three SIFs. In addition, Table 2 compares the SIFs relative errors with Peng et al. [72], when the analytical SIF is non-nil. The enriched formulation provides lower errors for both cases in all SIFs. Specifically, for K_I and K_{III}, an improvement of one order of magnitude is found in the relative error.

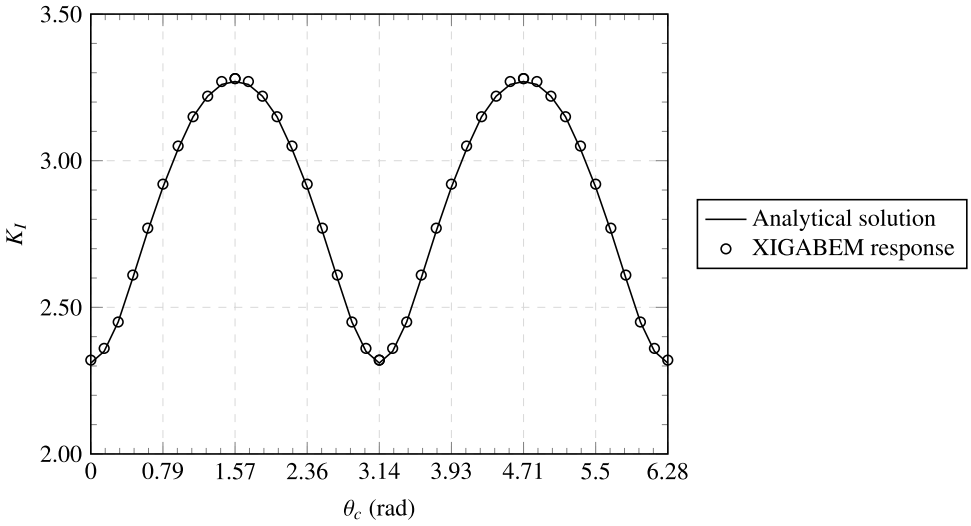

Fig. 16. Stress intensity factor K_I for in-plane elliptical crack.

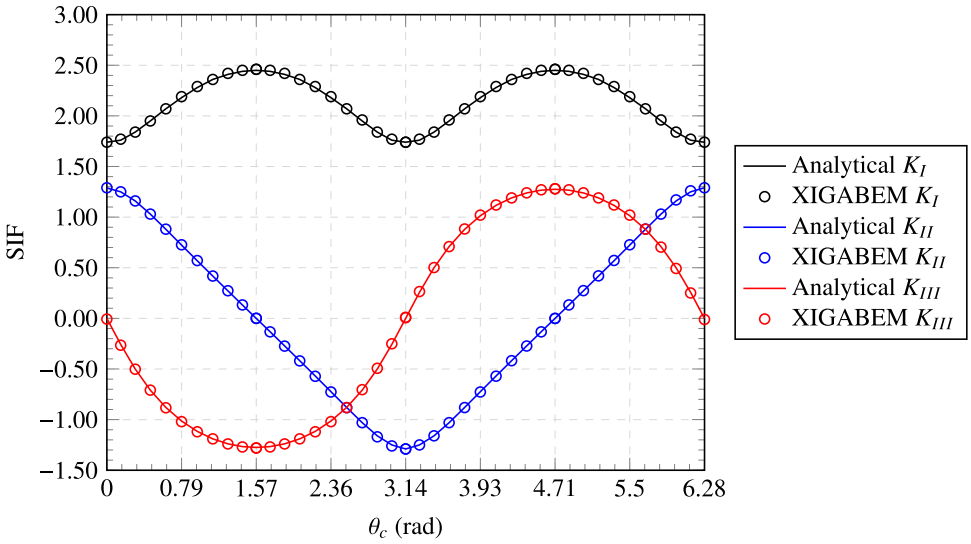

Fig. 17. Stress intensity factors for elliptical crack inclined by $\pi/6$ rad.

Table 2
Relative error for SIFs in elliptical crack inclined by $\theta_i = \pi/6$.

		VCCI [72]	M integral [72]	XIGABEM
$\theta_c = 0$	K_I	4.56e−2	1.53e−2	5.53e−04
	K_{II}	4.14e−2	1.28e−2	4.83e−03
	K_{III}	–	–	–
$\theta_c = \pi/2$	K_I	8.28e−3	2.21e−2	1.89e−03
	K_{II}	–	–	–
	K_{III}	6.88e−3	5.96e−2	1.77e−03

4.3. Prism with edge crack: pure mode analysis

This application consists of a finite prismatic solid with a centred crack of geometry defined in Fig. 18 and of material properties $E = 1.0$ and $\nu = 0.0$. We consider the pure mode behaviour, allowing us to make use of known analytical solutions as appropriate in order to elicit information about the numerical performance of the XIGABEM formulation. The upper face ($-1.0 \leq x_1 \leq 1.0$, $x_2 = 1.0$, $0.0 \leq x_3 \leq 2.0$), lower face ($-1.0 \leq x_1 \leq 1.0$, $x_2 = -1.0$, $0.0 \leq x_3 \leq 2.0$), front face ($x_1 = 1.0$, $-1.0 \leq x_2 \leq 1.0$, $0.0 \leq x_3 \leq 2.0$)

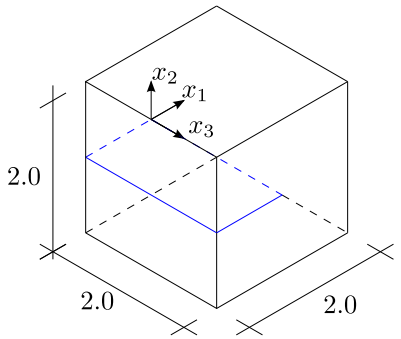

Fig. 18. Geometry of prismatic block with edge crack.

and back faces ($x_1 = -1.0$, $-1.0 \leq x_2 \leq 1.0$, $0.0 \leq x_3 \leq 2.0$,) are given displacement boundary conditions, while all other faces in the external boundary have prescribed traction. Since the analytical expressions for the mechanical behaviour are known for each opening mode [78], they are directly applied in the BIEs, as described in Appendix A. The displacement and stress values for this application are:

$$\begin{Bmatrix} u_1 \\ u_2 \\ u_3 \end{Bmatrix} = \frac{1}{2\mu}\sqrt{\frac{r^t}{2\pi}} \begin{bmatrix} \cos\left(\frac{\theta^t}{2}\right)(\kappa - \cos\theta^t) & \sin\left(\frac{\theta^t}{2}\right)(\kappa + 2 + \cos\theta^t) & 0 \\ \sin\left(\frac{\theta^t}{2}\right)(\kappa - \cos\theta^t) & -\cos\left(\frac{\theta^t}{2}\right)(\kappa - 2 + \cos\theta^t) & 0 \\ 0 & 0 & 4\sin\left(\frac{\theta^t}{2}\right) \end{bmatrix} \begin{Bmatrix} K_I \\ K_{II} \\ K_{III} \end{Bmatrix}$$

$$\begin{Bmatrix} \sigma_{11} \\ \sigma_{22} \\ \sigma_{33} \\ \sigma_{12} \\ \sigma_{13} \\ \sigma_{23} \end{Bmatrix} = \frac{1}{\sqrt{2\pi r^t}} \left\{ \begin{Bmatrix} \cos\left(\frac{\theta^t}{2}\right)\left[1 - \sin\left(\frac{\theta^t}{2}\right)\sin\left(\frac{3\theta^t}{2}\right)\right] \\ \cos\left(\frac{\theta^t}{2}\right)\left[1 + \sin\left(\frac{\theta^t}{2}\right)\sin\left(\frac{3\theta^t}{2}\right)\right] \\ 2\nu\cos\left(\frac{\theta^t}{2}\right) \\ \sin\left(\frac{\theta^t}{2}\right)\cos\left(\frac{\theta^t}{2}\right)\cos\left(\frac{3\theta^t}{2}\right) \\ 0 \\ 0 \end{Bmatrix} K_I + \begin{Bmatrix} -\sin\left(\frac{\theta^t}{2}\right)\left[2 + \cos\left(\frac{\theta^t}{2}\right)\sin\left(\frac{3\theta^t}{2}\right)\right] \\ \sin\left(\frac{\theta^t}{2}\right)\cos\left(\frac{\theta^t}{2}\right)\cos\left(\frac{3\theta^t}{2}\right) \\ -2\nu\sin\left(\frac{\theta^t}{2}\right) \\ \cos\left(\frac{\theta^t}{2}\right)\left[1 - \sin\left(\frac{\theta^t}{2}\right)\sin\left(\frac{3\theta^t}{2}\right)\right] \\ 0 \\ 0 \end{Bmatrix} K_{II} + \begin{Bmatrix} 0 \\ 0 \\ 0 \\ 0 \\ \cos\theta^t\sin\left(\frac{\theta^t}{2}\right) - \sin\theta^t\cos\left(\frac{\theta^t}{2}\right) \\ \sin\theta^t\sin\left(\frac{\theta^t}{2}\right) + \cos\theta^t\cos\left(\frac{\theta^t}{2}\right) \end{Bmatrix} K_{III} \right\} \tag{29}$$

The numerical analysis via XIGABEM is performed on a NURBS mesh with 9 patches, in which 7 patches define the external boundary and 2 patches represent the opposing crack faces. Fig. 19(a) presents the extended IGABEM mesh. It should be noted that the lateral faces do not align with the crack faces, since the Williams-based enrichment functions capture the discontinuous solution independently of the mesh. The upper and lower crack faces are given the crack front enrichment, which allows the direct determination of the SIFs. To compare the convergence rate of the XIGABEM against the standard IGABEM formulation, the numerical responses for the conventional IGABEM method utilises a mesh containing 15 NURBS patches, as shown in Fig. 19(b). The increased number of patches derives from the need for mesh alignment at the intersections between the external boundary and the crack on lateral faces.

This application considers each crack opening mode separately so that it is possible to evaluate the influence of all terms from the enrichment functions. The boundary conditions for the pure mode $M = I, II, III$ utilise Eq. (29) with $K_M = 1.0$ and 0.0 for other K's. Fig. 20 presents the deformed shape for each crack opening mode for both XIGABEM and standard IGABEM formulations. Discontinuous displacements are evident at the lateral faces in the IGABEM model, since multiple discontinuously defined NURBS patches represent these faces, and therefore no continuity between them is imposed. This is naturally circumvented by the extended IGABEM approach, because it does not require mesh alignment, and this can be seen in the results with continuity maintained over the face. Further, unlike in the standard IGABEM, the effect of the tying equations enforces displacement continuity over the crack front in the enriched XIGABEM scheme.

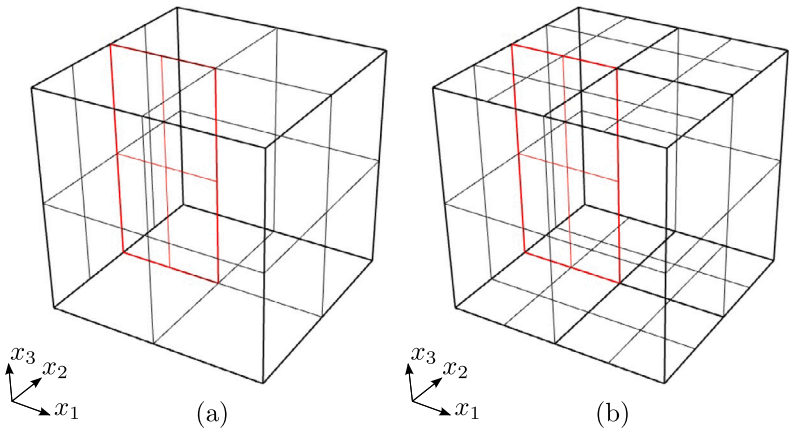

Fig. 19. Mesh for prismatic block with edge crack for (a) XIGABEM analysis and (b) standard IGABEM approach.

Table 3
Average values for SIFs in each pure mode loading case of prism with edge crack.

	Degrees of freedom	avg. $\|K_I\|$	avg. $\|K_{II}\|$	avg. $\|K_{III}\|$
Mode I	639	1.00057	5.84e−07	2.66e−06
	1275	0.99979	9.66e−06	2.95e−05
	2175	0.99991	9.17e−06	1.96e−05
Mode II	639	7.06e−07	1.00125	1.70e−02
	1275	7.55e−05	1.00050	2.21e−03
	2175	8.36e−07	1.00032	1.39e−04
Mode III	639	7.19e−07	7.06e−04	0.99579
	1275	1.51e−03	7.92e−04	1.00228
	2175	6.81e−06	2.74e−04	0.99991

The convergence analysis shown in Fig. 21 presents the error comparison for both XIGABEM and IGABEM approaches for each crack mode. For all modes, the standard IGABEM convergence rate is around 0.6, explained by the square-root nature of the fracture mechanics solution that is not captured by the NURBS basis functions (neither in the crack faces nor in the lateral faces). On the other hand, this behaviour is injected into the extended IGABEM approximation, which results in better convergence for all three modes when compared against the standard formulation. It is evident from Fig. 21 that different convergence rates are found for the different modes. We note that some caution is needed in interpreting convergence rates for XIGABEM, since the important square root behaviour is included in the coarsest models, but not improved in later refinements which add only the smooth NURBS basis functions. In addition, Fig. 22 presents the comparison of the condition number of the $\mathbf{A}$ matrix for both XIGABEM and IGABEM approaches. For each approach, the condition number is the same for all modes, since a change in the boundary conditions only affects the right-hand side vector. Through this analysis, it can be seen that the enrichment strategies cause a consequent increase in the condition number. Nevertheless, the degree of ill-conditioning for the XIGABEM in this application is mild and does not jeopardise the accuracy of the system solution.

In Table 3 we study the SIF results obtained directly from the XIGABEM solution vector $\mathbf{x}$. The table presents the average value for the absolute SIFs along the crack front for all crack opening modes. All SIFs match closely with the expected value for each pure mode loading, and the errors reduce with mesh refinement. For all cases, the most refined mesh provides the associated SIF for its pure mode loading with errors below 4.10^{-4}. This provides evidence that the proposed formulation is capable of delivering SIFs to high accuracy without the requirement for post-processing tasks, as J-Integral.

4.4. Prism with edge crack: uniform load

The fourth application of this study deals with the numerical analysis of a finite prismatic block under uniform traction $\sigma_0 = 1.0$ at its ends. Fig. 23 presents its geometry and boundary conditions, in which the displacements in the highlighted region are responsible for preventing rigid body motion. The material properties are: Young modulus $E = 1000.0$ and Poisson ratio $\nu = 0.3$. This application does not have an analytical response, which requires its comparison against reference solutions obtained by other authors using different numerical methods. Also, it is reasonable to expect plane-strain behaviour at the middle of the crack front $z = 3.75$, at which the correspondent K_I is [85]:

$$K_I = \sigma_0 \sqrt{\pi a} F(a/b)$$
$$F(a/b) = 1.122 - 0.231 \left(\frac{a}{b}\right) + 10.550 \left(\frac{a}{b}\right)^2 - 21.710 \left(\frac{a}{b}\right)^3 + 30.382 \left(\frac{a}{b}\right)^4 \tag{30}$$

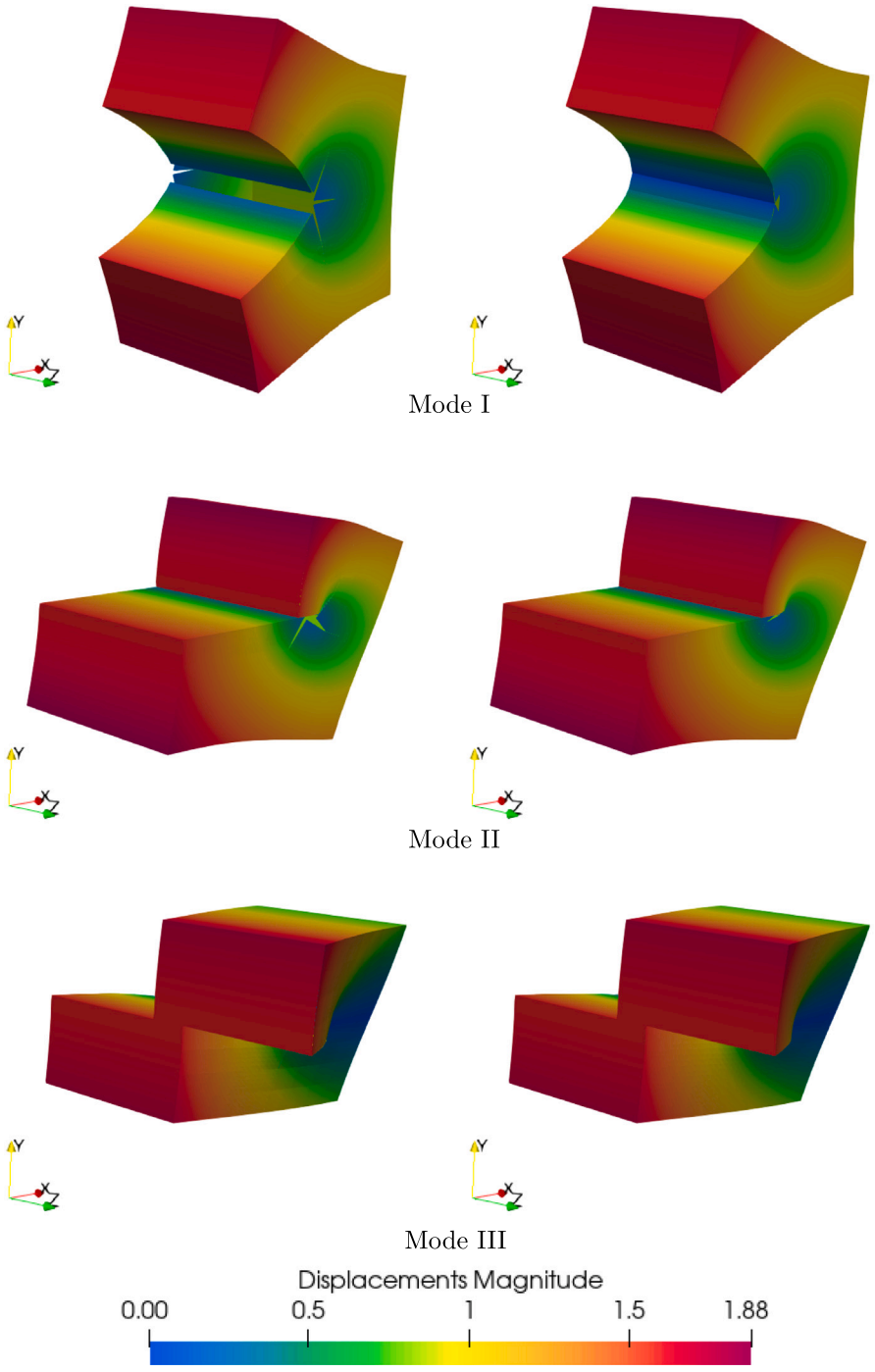

Fig. 20. Deformed shape for each pure crack loading where standard IGABEM results are on the left-hand side while the XIGABEM responses are on the right-hand side.

Initially, the crack surfaces are given only the SIF enrichment, and the corresponding mesh presented in Fig. 24(a) consists of 17 NURBS surfaces, of degree $p = q = 1$ for the external boundary and $p = q = 2$ for the crack surfaces. In this mesh, all surfaces must align with the crack, which places additional demands on the CAD model to satisfy this requirement. Additionally, the fully enriched analysis considers the SIF enrichment on the crack faces, the Williams-based enrichment on the lateral faces and the Heaviside enrichment on the fully cut face, which reduces the amount of NURBS surfaces to 10, as depicted in Fig. 24(b). Again, the NURBS basis functions are of degree $p = q = 1$ on the external boundary faces and $p = q = 2$ on the crack faces. In this application there is

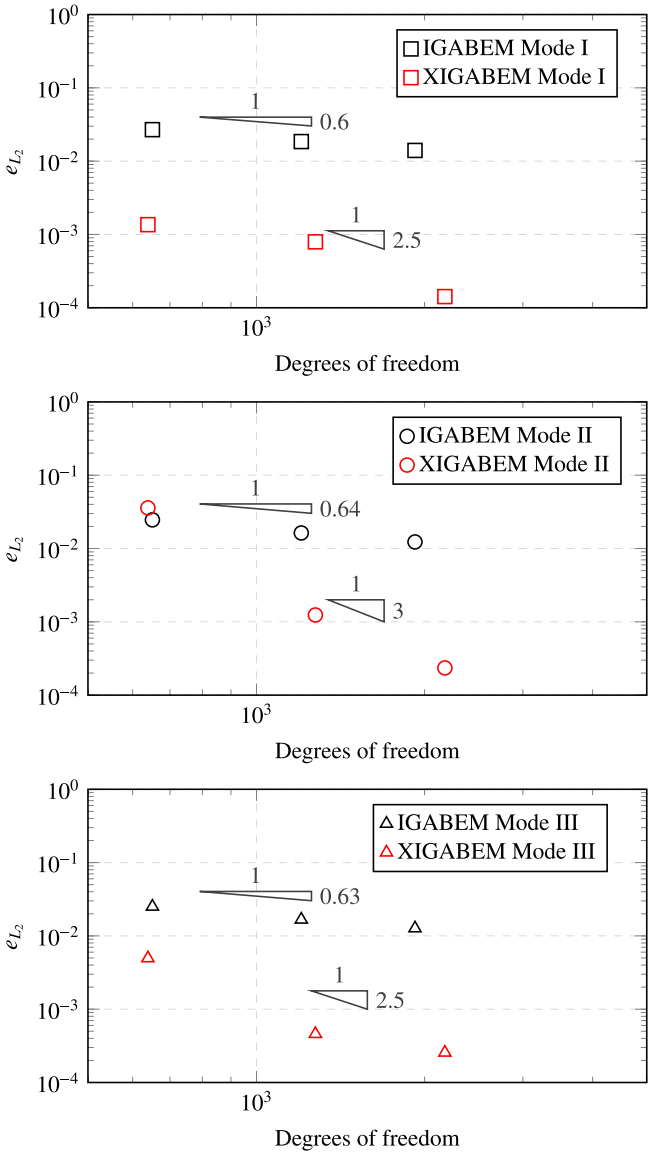

Fig. 21. L_2 norm of error in displacements for prismatic block with edge crack.

a plane-stress/plane-strain transition at the crack front close to the lateral faces. In order to study this behaviour, and therefore the influence of the Kolosov constant on the results, for the fully enriched model two different analyses consider the Kolosov constant prescribed for plane-stress and plane-strain scenarios. Therefore, three different models are compared against reference solutions using IGABEM by Cordeiro and Leonel [73] and Lagrangian BEM by Mi and Aliabadi [37], and against the 2-D plane-strain solution. It is relevant to mention that the 2-D equivalent solution for this problem does not hold for the entire crack front. However, the aforementioned references have shown that it becomes a suitable comparison close to the crack front centre, where the plane-strain behaviour is more prominent.

The number of degrees of freedom for each analysis are 3996 and 2787 for the model with only SIF enrichment and for the fully enriched model, respectively. In addition, the models of Cordeiro and Leonel [73] comprise 3273 and 5121 degrees of freedom for two different refinement levels, while Mi and Aliabadi [37] do not provide their model sizes. The normalised K_I comparison in Fig. 25 demonstrates that the crack front enrichment is capable of directly determining the SIF for all scenarios in broad agreement with other results in the literature. At the crack front coordinate $z = 3.75$, the XIGABEM model with only crack front enrichment has a relative difference in K_I of 2.0% in comparison to the 2-D plane-strain solution, while the fully enriched models give rise to discrepancies of 0.52% and 0.96% when using plane-strain and plane-stress Kolosov constants at the Williams-based enrichment, respectively. Therefore, it is noticeable that capturing the square-root behaviour over the lateral faces improves the SIF determination. On the other hand, it is interesting that the Kolosov parameter being considered as plane-stress on lateral faces forces

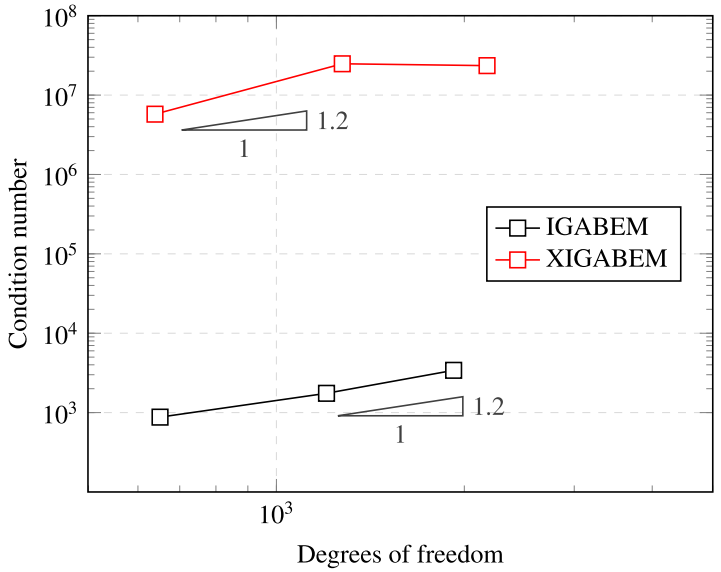

Fig. 22. Condition number growth for prismatic block with edge crack.

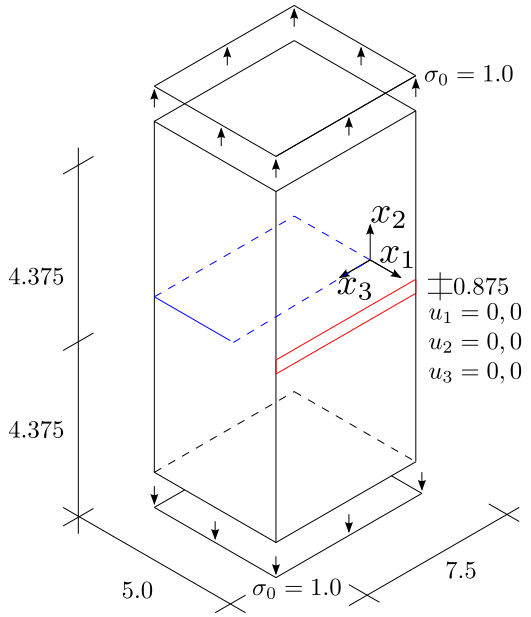

Fig. 23. Geometry and boundary conditions for prismatic specimen under uniform traction.

the overall K_I variation to be lower than the plane-strain case. Still, both situations lead to an accurate result in comparison to other numerical methods and the handbook two-dimensional solution. Moreover, the fully enriched models deliver higher accuracy than the standard IGABEM model with 3273 degrees of freedom, whose difference was 1.93%. It must be noticed that the present study and Cordeiro and Leonel [73] utilised $\nu = 0.3$ while Mi and Aliabadi [37] used $\nu = \frac{1}{3}$. The numerical analysis of this application with XIGABEM has obtained up to only 0.5% difference in SIF at the centre of the crack. In summary, it is possible to obtain higher accuracy from coarser models, providing evidence of a gain in solution accuracy available using the extended IGABEM approach.

5. Concluding remarks

This study proposes enrichment strategies for the isogeometric boundary element method for three-dimensional linear elastic fracture mechanics. Then, the eXtended Isogeometric Boundary Element Method was used for the numerical analysis of 3-D cracked bodies.

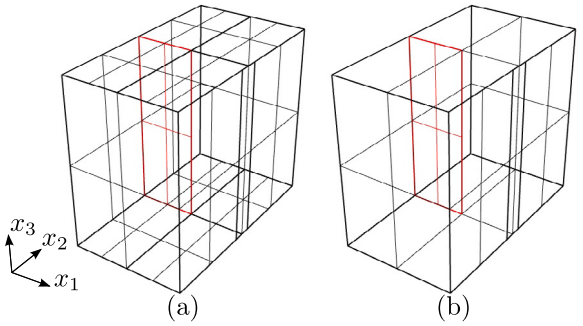

Fig. 24. Isogeometric mesh for prismatic block under uniform traction, in which (a) XIGABEM mesh with only the SIF enrichment, and (b) fully enriched model.

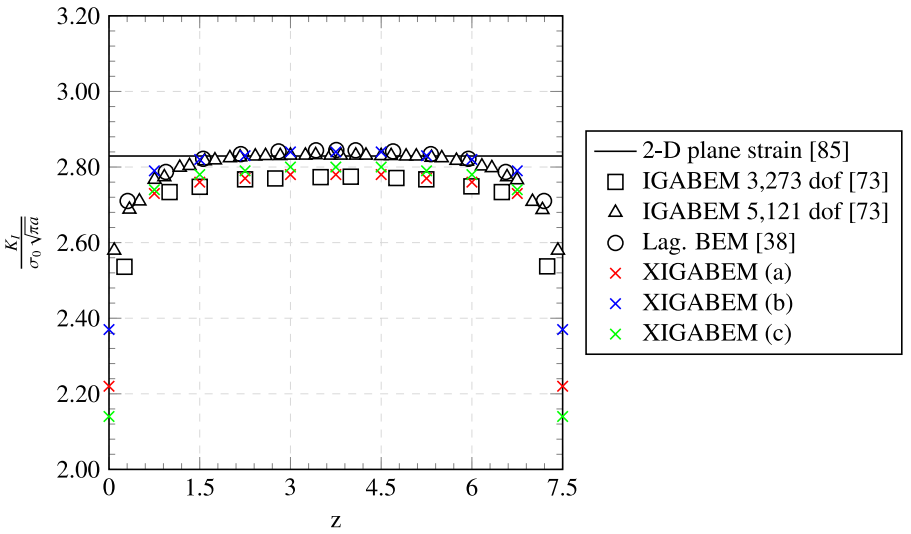

Fig. 25. Stress intensity factors along crack front, in which XIGABEM (a) is the model with only the crack front enrichment, XIGABEM (b) and (c) are the fully enriched models with Kosolov constant set as plane strain and plane stress, respectively.

Two different functions were responsible for enriching the expansion of the displacement field to incorporate the expected behaviour of the fracture mechanics: the Heaviside and the Williams expansion. While the former permits the direct representation of discontinuities for fully cut faces, the latter allowed the representation of the $\sqrt{\rho}$ behaviour of displacements near the crack front. In addition, two different approaches consider the Williams solution: one on boundary faces partially cut by the crack, and another over the crack surfaces themselves. For the boundary faces, besides incorporating a behaviour that was not captured by the standard NURBS functions, this strategy precludes the need for a re-meshing task on this face. In addition, the Williams-based enrichment for crack faces introduces the stress intensity factors directly as system unknowns, found in the solution vector, which removes a post-processing task for their determination.

As a consequence of enriching the displacement field, the additional unknowns require new equations to recover a square system. This may be achieved by the use of the Traction Boundary Integral Equation at the same position as the collocation points whose basis functions were enriched, and for the SIF enrichment a tying constraint equation is responsible for this task. With the additional benefit of the removal of a non-physical displacement discontinuity at the crack front that occurs in the Lagrangian BEM and IGABEM.

Results showed that the convergence rate improves for the XIGABEM in comparison to the standard IGABEM in various applications. In addition, it was possible to accurately extract the SIFs for problems containing straight and curved crack fronts directly from the additional unknowns introduced by the crack front enrichment. The comparison with literature applications also showed an improvement in the SIF determination.

This work demonstrated the feasibility and fundamental numerical analysis of the proposed scheme. Several enhancements will be possible for researchers to follow up. For example, instead of applying enrichment to the entirety of a surface partially intersected by a crack, we believe it will be possible to reduce the number of degrees of freedom by restricting the size of the enrichment zone on these faces. Also, the combination of Heaviside and Williams-based strategies on partially cut faces, will also be an interesting extension. Additionally, crack growth procedures based on extended IGABEM can also be relevant for the numerical analysis of

cracked complex engineering components. These topics are work in progress to extend the state of art of the fracture mechanics analysis under XIGABEM.

CRediT authorship contribution statement

Matheus Rocha: Writing – review & editing, Writing – original draft, Software, Methodology, Investigation, Conceptualization. **Jon Trevelyan:** Writing – review & editing, Supervision, Methodology, Investigation, Conceptualization. **Edson Denner Leonel:** Writing – review & editing, Supervision, Methodology, Investigation, Funding acquisition, Conceptualization.

Declaration of competing interest

The authors declare that they have no known competing financial interests or personal relationships that could have appeared to influence the work reported in this paper.

Data availability

Data will be made available on request.

Acknowledgements

Sponsorship of this research project by the grants no 2019/18795-6 and 2022/00714-2 by the São Paulo Research Foundation (FAPESP) are greatly appreciated.

Appendix A. Three-dimensional isogeometric boundary element method

This appendix presents the IGABEM formulation for three-dimensional linear elasticity and for fracture mechanics. Further details can be found in the "Isogeometric Boundary Element Method" book [62]. The Boundary Element Method consists of utilising integral equations written solely at the solid boundary to determine its mechanical fields. Consider a three-dimensional body with domain Ω, boundary $\Gamma = \Gamma_u \cup \Gamma_t$, in which Γ_u and Γ_t contain Dirichlet and Neumann boundary conditions, respectively, linear-elastic isotropic mechanical behaviour and absence of body forces. For this body, the Displacement Boundary Integral Equation (DBIE) obtains its displacements u_k on a collocation point $\hat{\mathbf{x}}$ as:

$$c_{\ell k}(\hat{\mathbf{x}})u_k(\hat{\mathbf{x}}) + \int_\Gamma T^*_{\ell k}(\mathbf{x},\hat{\mathbf{x}})u_k(\mathbf{x})\,d\Gamma = \int_\Gamma U^*_{\ell k}(\mathbf{x},\hat{\mathbf{x}})t_k(\mathbf{x})\,d\Gamma \tag{A.1}$$

in which $\mathbf{x}$ is a field point on the boundary, $c_{\ell k}(\hat{\mathbf{x}})$ is the jump term associated with the position of $\hat{\mathbf{x}}$, assuming the value of $\delta_{\ell k}$ when $\hat{\mathbf{x}} \in \Omega$ and $0.5\delta_{\ell k}$ when $\hat{\mathbf{x}}$ is on a smooth portion of boundary Γ, being $\delta_{\ell k}$ the Kronecker delta. u_k and t_k are the displacements and tractions, respectively, and $U^*_{\ell k}$ and $T^*_{\ell k}$ denote the linear elasticity fundamental solutions, given by:

$$\begin{aligned} U^*_{\ell k}(\mathbf{x},\hat{\mathbf{x}}) &= \frac{1}{16\pi\mu\,(1-\nu)\,r}\left[(3-4\nu)\,\delta_{\ell k} + r_{,\ell}r_{,k}\right] \\ T^*_{\ell k}(\mathbf{x},\hat{\mathbf{x}}) &= \frac{-1}{8\pi\,(1-\nu)\,r^2}\left\{\frac{\partial r}{\partial \mathbf{n}}\left[(1-2\nu)\,\delta_{\ell k} + 3r_{,\ell}r_{,k}\right] - (1-2\nu)\left(r_{,\ell}n_k + r_{,k}n_\ell\right)\right\} \end{aligned} \tag{A.2}$$

in which $\mu = \frac{E}{2(1+\nu)}$, E and ν are the material properties shear modulus, Young Modulus and Poisson ratio, respectively. These expressions use the distance vector $\mathbf{r} = \mathbf{x} - \hat{\mathbf{x}}$ between $\hat{\mathbf{x}}$ and $\mathbf{x}$, its derivatives, and the normal outward vector $\mathbf{n}$ at the field point. Given the singular aspect of the fundamental solutions, the first integration in Eq. (A.1) is strongly singular when a collocation point lies on the boundary, which requires the *Cauchy Principal Value* (CPV) for its regularisation [42], indicated by $\fint$.

The Traction Boundary Integral Equation (TBIE) arises from the differentiation of Eq. (A.1) with respect to the point $\hat{\mathbf{x}}$. For $\hat{\mathbf{x}}$ in a smooth boundary, the TBIE is:

$$c_{\ell k}(\hat{\mathbf{x}})\,t_k(\hat{\mathbf{x}}) + n_\ell(\hat{\mathbf{x}})\fint_\Gamma S^*_{k\ell j}(\mathbf{x},\hat{\mathbf{x}})u_k(\mathbf{x})\,d\Gamma = n_\ell(\hat{\mathbf{x}})\fint_\Gamma D^*_{k\ell j}t_k(\mathbf{x})(\mathbf{x},\hat{\mathbf{x}})\,d\Gamma \tag{A.3}$$

in which the fundamental solutions $S^*_{k\ell j}$ and $D^*_{k\ell j}$ are:

$$\begin{aligned} D^*_{k\ell j}(\mathbf{x},\hat{\mathbf{x}}) &= \frac{1}{8\pi(1-\nu)r^2}\left[(1-2\nu)(\delta_{k\ell}r_{,j} + \delta_{jk}r_{,\ell} - \delta_{\ell j}r_{,k}) + 3(r_{,\ell}r_{,j}r_{,k})\right] \\ S^*_{k\ell j}(\mathbf{x},\hat{\mathbf{x}}) &= \frac{\mu}{4\pi(1-\nu)r^3}\{3\frac{\partial r}{\partial n}[(1-2\nu)\delta_{\ell j}r_{,k} + \nu(\delta_{\ell k}r_{,j} + \delta_{jk}r_{,\ell}) - 5r_{,\ell}r_{,j}r_{,k}] \\ &+3\nu(n_\ell r_{,j}r_{,k} + n_j r_{,\ell}r_{,k}) + (1-2\nu)(3n_k r_{,\ell}r_{,j} + n_j\delta_{\ell k} + n_\ell\delta_{jk}) - (1-4\nu)n_k\delta_{\ell j}\} \end{aligned} \tag{A.4}$$

The kernel $D^*_{k\ell j}$ is strongly singular and regularised by the CPV, while the hypersingular nature of $S^*_{k\ell j}$ requires the integration in the *Hadamard Finite Part* sense, represented by $\fint$ in Eq. (A.3). For brevity, the arguments of the fundamental solutions will be omitted henceforth.

In this study, the basis functions describing Non-Uniform Rational B-Splines (NURBS) are used to interpolate both geometry and mechanical fields. This choice enables an exact description of conic surfaces, such as spheres and ellipses. Moreover, the boundary-only aspect of the integral equations allows the direct import of the CAD drawing, which precludes a costly mesh generation task in the analyses [50]. In addition, NURBS basis functions possess several important properties for the numerical methods, such as Partition of Unity, non-negativity, local support, existence of all derivatives of R_i in the interior of a knot span and being $p-k$ times continuously differentiable at a knot, with k denoting its multiplicity, among other characteristics [80].

In order to describe the boundary Γ we make use of NURBS surfaces; here, the basis functions are derived from a tensor product between two univariate NURBS curves [50,80]. The univariate NURBS basis functions are built recursively based on the B-spline basis using the Cox-de-Boor formula [88–90] and weights w_i of each control point as:

$$\begin{aligned}
\phi_i(\xi) &= \frac{N_i(\xi)w_i}{\sum_{k=1}^{n} N_k(\xi)w_k} \\
N_{i,0}(\xi) &= \begin{cases} 1 & \xi_i \le \xi < \xi_{i+1} \\ 0 & \text{otherwise} \end{cases} \\
N_{i,p}(\xi) &= \frac{\xi-\xi_i}{\xi_{i+p}-\xi_i} N_{i,p-1}(\xi) + \frac{\xi_{i+p+1}-\xi}{\xi_{i+p+1}-\xi_{i+1}} N_{i+1,p-1}(\xi)
\end{aligned} \tag{A.5}$$

in which a NURBS curve of degree p has a non-decreasing knot-vector $\Xi = \{\xi_1, \xi_2, \dots, \xi_k\}$. Then, by taking two uni-variate NURBS curves, one with degree p, amount of basis functions n and knot-vector $\Xi_1 = \left\{\xi_1^1, \xi_1^2, \dots, \xi_1^{n+p+1}\right\}$ in ξ_1 direction and another with degree q, amount of basis function m and knot-vector $\Xi_2 = \left\{\xi_2^1, \xi_2^2, \dots, \xi_2^{m+q+1}\right\}$ in ξ_2 direction, the bi-variate basis function is:

$$\phi_\alpha(\xi_1,\xi_2) = \frac{N_i(\xi_1)M_j(\xi_2)w_{ij}}{\sum_{k=1}^{n}\sum_{l=1}^{m} N_k(\xi_1)M_l(\xi_2)w_{kl}} \tag{A.6}$$

in which α refers to the NURBS surface local index associated to the indices i and j of each univariate NURBS function, and w_{ij} is the corresponding weight. Based on these basis functions, it is possible to interpolate both geometry, represented by x_k^γ, and mechanical fields as:

$$\begin{aligned}
x_k^\gamma(\xi_1,\xi_2) &= \sum_{\alpha=1}^{n^\gamma} \phi_\alpha^\gamma(\xi_1,\xi_2) P_k^\alpha \\
u_k^\gamma(\xi_1,\xi_2) &= \sum_{\alpha=1}^{n^\gamma} \phi_\alpha^\gamma(\xi_1,\xi_2) d_k^\beta \\
t_k^\gamma(\xi_1,\xi_2) &= \sum_{\alpha=1}^{n^\gamma} \phi_\alpha^\gamma(\xi_1,\xi_2) p_k^\beta
\end{aligned} \tag{A.7}$$

in which d_k^β and p_k^β are displacement and traction parameters, β is a global index given by a connectivity function from γ and α, and $n^\gamma = (p^\gamma+1)*(q^\gamma+1)$ is the number of NURBS basis functions describing a patch γ. It should be noted that these coefficients do not have physical meaning, but are simply coefficients (with the appropriate units) from which the geometry, displacement and traction can be recovered using (A.7). It is worth mentioning that this aspect requires special procedures in applying non-constant boundary conditions.

The substitution of Eq. (A.7) in Eq. (A.1) and Eq. (A.3), both written for a collocation point on the boundary, leads to the discretised form of these BIEs, as:

$$\begin{aligned}
c_{\ell k}(\hat{\mathbf{x}}) \sum_{\alpha=1}^{n^\gamma} \phi_\alpha^{\hat{\gamma}}(\hat{\mathbf{x}}) d_k^\beta + \sum_{\gamma=1}^{NS} \oint_{\Gamma_\gamma} T_{\ell k}^* \sum_{\alpha=1}^{n^\gamma} \phi_\alpha^\gamma(\xi_1,\xi_2) d_k^\beta \, d\Gamma_\gamma \\
= \sum_{\gamma=1}^{NS} \int_{\Gamma^\gamma} U_{\ell k}^* \phi_\alpha^\gamma(\xi_1,\xi_2) p_k^\beta \, d\Gamma_\gamma \\
c_{\ell k}(\hat{\mathbf{x}}) \sum_{\alpha=1}^{n^\gamma} \phi_\alpha^{\hat{\gamma}}(\hat{\mathbf{x}}) p_k^\beta + n_\ell(\hat{\mathbf{x}}) \sum_{\gamma=1}^{NS} \oint_{\Gamma_\gamma} S_{k\ell j}^* \sum_{\alpha=1}^{n^\gamma} \phi_\alpha^\gamma(\xi_1,\xi_2) d_k^\beta \, d\Gamma_\gamma \\
= n_\ell(\hat{\mathbf{x}}) \sum_{\gamma=1}^{NS} \oint_{\Gamma_\gamma} D_{k\ell j}^* \sum_{\alpha=1}^{n^\gamma} \phi_\alpha^\gamma(\xi_1,\xi_2) p_k^\beta \, d\Gamma_\gamma
\end{aligned} \tag{A.8}$$

in which $\hat{\gamma}$ is the NURBS surface that contains the collocation point and NS accounts for the amount of NURBS surfaces in the discretisation. The numerical integration makes use of the mapping between each bivariate knot-span $[\xi_1^i, \xi_1^{i+1}] \times [\xi_2^j, \xi_2^{j+1}]$ and the

Gauss–Legendre integration space $\{\hat{\xi}_1, \hat{\xi}_2 \in \Lambda \mid \Lambda = [-1;1]\times[-1;1]\}$ as:

$$\begin{aligned}
\xi_1 &= \frac{(\xi_1^{i+1} - \xi_1^i)\,\hat{\xi}_1 + (\xi_1^{i+1} + \xi_1^i)}{2} \\
\xi_2 &= \frac{(\xi_2^{j+1} - \xi_2^j)\,\hat{\xi}_2 + (\xi_2^{j+1} + \xi_2^j)}{2} \\
J &= \left\| \frac{\partial \mathbf{r}}{\partial \xi_1} \times \frac{\partial \mathbf{r}}{\partial \xi_2} \right\| \frac{(\xi_1^{i+1} - \xi_1^i)}{2} \frac{(\xi_2^{j+1} - \xi_2^j)}{2}
\end{aligned} \tag{A.9}$$

in which J is the Jacobian of the mapping between the physical space and the integration space. By substituting the mappings into Eq. (A.8), it becomes:

$$\begin{aligned}
c_{\ell k}(\hat{\mathbf{x}}) \sum_{\alpha=1}^{n^\gamma} \phi_\alpha^{\hat{\gamma}}(\hat{\mathbf{x}}) d_k^\beta + \sum_{\gamma=1}^{NS} \underline{\mathrm{T}}^{*\alpha\gamma}_{\ell k}\, d_k^\beta &= \sum_{\gamma=1}^{NS} \underline{\mathrm{U}}^{*\alpha\gamma}_{\ell k}\, p_k^\beta \\
c_{\ell k}(\hat{\mathbf{x}}) \sum_{\alpha=1}^{n^\gamma} \phi_\alpha^{\hat{\gamma}}(\hat{\mathbf{x}}) p_k^\beta + n_\ell(\hat{\mathbf{x}}) \sum_{\gamma=1}^{NS} \underline{\mathrm{S}}^{*\alpha\gamma}_{k\ell j}\, d_k^\beta &= n_\ell(\hat{\mathbf{x}}) \sum_{\gamma=1}^{NS} \underline{\mathrm{D}}^{*\alpha\gamma}_{k\ell j}\, p_k^\beta
\end{aligned} \tag{A.10}$$

in which $\underline{T}^{*\alpha\gamma}_{\ell k}$, $\underline{U}^{*\alpha\gamma}_{\ell k}$, $\underline{S}^{*\alpha\gamma}_{k\ell j}$ and $\underline{D}^{*\alpha\gamma}_{k\ell j}$ are:

$$\begin{aligned}
\underline{\mathrm{T}}^{*\alpha\gamma}_{\ell k} &= \sum_{\mathrm{ks}=1}^{n^\gamma_{\mathrm{ks}}} \sum_{\alpha=1}^{n^\gamma} \int_\Lambda T^*_{\ell k} \phi^\gamma_\alpha J^{\mathrm{ks}}_\gamma \, d\Lambda \\
\underline{\mathrm{U}}^{*\alpha\gamma}_{\ell k} &= \sum_{\mathrm{ks}=1}^{n^\gamma_{\mathrm{ks}}} \sum_{\alpha=1}^{n^\gamma} \int_\Lambda U^*_{\ell k} \phi^\gamma_\alpha J^{\mathrm{ks}}_\gamma \, d\Lambda \\
\underline{\mathrm{S}}^{*\alpha\gamma}_{k\ell j} &= \sum_{\mathrm{ks}=1}^{n^\gamma_{\mathrm{ks}}} \sum_{\alpha=1}^{n^\gamma} \int_\Lambda S^*_{k\ell j} \phi^\gamma_\alpha J^{\mathrm{ks}}_\gamma \, d\Lambda \\
\underline{\mathrm{D}}^{*\alpha\gamma}_{k\ell j} &= \sum_{\mathrm{ks}=1}^{n^\gamma_{\mathrm{ks}}} \sum_{\alpha=1}^{n^\gamma} \int_\Lambda D^*_{k\ell j} \phi^\gamma_\alpha J^{\mathrm{ks}}_\gamma \, d\Lambda
\end{aligned} \tag{A.11}$$

in which ks is the integrated knot-span and n^γ_{ks} is the number of knot-spans in patch γ. Moreover, when the collocation point does not lie on the element being integrated, a standard Gauss–Legendre quadrature is sufficient to evaluate accurately the integral. On the other hand, the Singularity Subtraction Technique (SST) [42,43] can facilitate the integration for the strongly singular and hypersingular kernels. The expressions associated with the expansions required are available in [73]; the basis functions are expanded in a Taylor Series in polar coordinates. The enrichment strategies used in this study will require the corresponding derivatives highlighted in Appendix B to perform the SST of the arising kernels. In addition, it is noted that this procedure requires C^1 continuity of the basis functions at the collocation point for the correct use of the hypersingular traction integral equation.

Once Eq. (A.10) establishes a relationship between the mechanical fields at a given collocation point, it results in a set of only three equations. However, the discretised linear elasticity problem has $3n_d$ and $3n_t$ displacement and traction coefficients, respectively. Half of these variables comes from boundary conditions, while the another half is unknown. Therefore, choosing n different collocation points positions enables the obtaining of all linearly independent equations needed for a well-posed system. The Greville Abscissae (GA) [91] are commonly applied to define the parametric coordinate of each collocation point in the IGABEM context [72–75]. For each basis function, the corresponding pair $(\hat{\xi}_1, \hat{\xi}_2)^\alpha = (\hat{\xi}_1^i, \hat{\xi}_2^j)$ is:

$$\begin{aligned}
\hat{\xi}_1^i &= \frac{\sum_{s=i+1}^{i+p} \xi_1^s}{p} \\
\hat{\xi}_2^j &= \frac{\sum_{s=j+1}^{j+q} \xi_2^s}{q}
\end{aligned} \tag{A.12}$$

in which ξ_1^s and ξ_2^s refer to the knot-vector of each univariate NURBS curve that generates the NURBS surface. In order to satisfy the continuity requirements of the TBIE, some collocation points given by the GA approach need to be re-positioned to ensure that C^1 continuity in displacement exists at these points. One of the pair coordinates $(\hat{\xi}_1, \hat{\xi}_2)^\alpha$ is modified if it coincides with a limit of a knot-span $[\xi_1^i, \xi_1^{i+1}]$ and $[\xi_2^j, \xi_2^{j+1}]$, as:

$$\begin{aligned}
&\hat{\xi}_1^{i\,\mathrm{alt}} = \hat{\xi}_1^i + 0.1(\xi_1^{i+1} - \xi_1^i) \text{ when } \xi_1^i \text{ has } p \text{ or higher multiplicity} \\
&\hat{\xi}_1^{i+1\,\mathrm{alt}} = \hat{\xi}_1^{i+1} - 0.1(\xi_1^{i+1} - \xi_1^i) \text{ when } \xi_1^{i+1} \text{ has } p \text{ or higher multiplicity} \\
&\hat{\xi}_2^{j\,\mathrm{alt}} = \hat{\xi}_2^j + 0.1(\xi_2^{j+1} - \xi_2^j) \text{ when } \xi_2^j \text{ has } q \text{ or higher multiplicity} \\
&\hat{\xi}_2^{j+1\,\mathrm{alt}} = \hat{\xi}_2^{j+1} - 0.1(\xi_2^{j+1} - \xi_2^j) \text{ when } \xi_2^{j+1} \text{ has } q \text{ or higher multiplicity}
\end{aligned} \tag{A.13}$$

For fracture mechanics problems, the boundary is redefined as $\Gamma = \Gamma_u \cup \Gamma_t \cup \Gamma_+ \cup \Gamma_-$, in which Γ_+ and Γ_- are the upper and lower crack surfaces. For this body, the GA strategy within IGABEM positions the collocation points at the same geometrical positions on

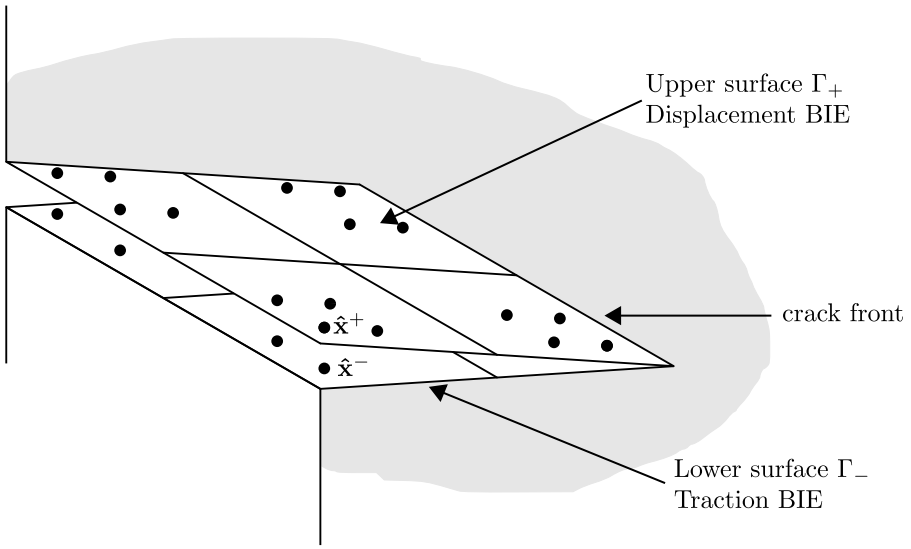

Fig. A.26. Application of each integral equation in the Dual BEM.

the opposing, coincident crack faces. Solely using the DBIE at two such coincident points leads to identical equations and hence an ill-posed system. This is classically overcome by the Dual BEM approach [31,37], which generates a linear system of linearly independent equations by the application of different boundary integral equations, the DBIE and the TBIE, on the collocation points over each opposing crack face, as illustrated in Fig. A.26. Therefore, the application of Eq. (A.10) for a collocation point $\hat{\mathbf{x}}$, $\hat{\mathbf{x}}^+$ and $\hat{\mathbf{x}}^-$, at the external boundary, upper crack face or lower crack face, respectively, results in:

$$
\begin{aligned}
c_{\ell k}(\hat{\mathbf{x}}) \sum_{\alpha=1}^{n^\gamma} \phi_\alpha^{\hat{\gamma}}(\hat{\mathbf{x}}) d_k^\beta + \sum_{\gamma=1}^{NS} \underline{\mathrm{T}}^{*\alpha\gamma}_{\ell k}\, d_k^\beta &= \sum_{\gamma=1}^{NS} \underline{\mathrm{U}}^{*\alpha\gamma}_{\ell k}\, p_k^\beta \\
c_{\ell k}(\hat{\mathbf{x}}^+) \sum_{\alpha=1}^{n^\gamma} \phi_\alpha^{\hat{\gamma}+}(\hat{\mathbf{x}}^+) d_k^\beta + c_{\ell k}(\hat{\mathbf{x}}^-) \sum_{\alpha=1}^{n^\gamma} \phi_\alpha^{\hat{\gamma}-}(\hat{\mathbf{x}}^-) d_k^\beta + \sum_{\gamma=1}^{NS} \underline{\mathrm{T}}^{*\alpha\gamma}_{\ell k}\, d_k^\beta &= \sum_{\gamma=1}^{NS} \underline{\mathrm{U}}^{*\alpha\gamma}_{\ell k}\, p_k^\beta \\
0.5\delta_{\ell k}(\hat{\mathbf{x}}^-) \sum_{\alpha=1}^{n^\gamma} \phi_\alpha^{\hat{\gamma}-}(\hat{\mathbf{x}}) p_k^\beta - 0.5\delta_{\ell k}(\hat{\mathbf{x}}^+) \sum_{\alpha=1}^{n^\gamma} \phi_\alpha^{\hat{\gamma}+}(\hat{\mathbf{x}}^+) p_k^\beta & \\
+ n_\ell(\hat{\mathbf{x}}^-) \sum_{\gamma=1}^{NS} \underline{\mathrm{S}}^{*\alpha\gamma}_{k\ell j}\, d_k^\beta = n_\ell(\hat{\mathbf{x}}) \sum_{\gamma=1}^{NS} \underline{\mathrm{D}}^{*\alpha\gamma}_{k\ell j}\, p_k^\beta &
\end{aligned}
\tag{A.14}
$$

in which jump terms arise in both equations applied to crack faces due to the limit analysis.

The IGABEM algebraic system for cracked bodies emerges by applying Eq. (A.14) at each collocation point obtained from Eq. (A.12) in matrix notation, as:

$$
\begin{bmatrix} \mathbf{H}^{\mathrm{eb}} \\ \mathbf{H}^{\mathrm{c}^+} \\ \mathbf{H}^{\mathrm{c}^-} \end{bmatrix} \begin{bmatrix} \mathbf{d}^{\mathrm{eb}} \\ \mathbf{d}^{\mathrm{c}^+} \\ \mathbf{d}^{\mathrm{c}^-} \end{bmatrix} = \begin{bmatrix} \mathbf{G}^{\mathrm{eb}} \\ \mathbf{G}^{\mathrm{c}^+} \\ \mathbf{G}^{\mathrm{c}^-} \end{bmatrix} \begin{bmatrix} \mathbf{p}^{\mathrm{eb}} \\ \mathbf{p}^{\mathrm{c}^+} \\ \mathbf{p}^{\mathrm{c}^-} \end{bmatrix}
\qquad \mathbf{Hd} = \mathbf{Gt}
\tag{A.15}
$$

in which $\mathbf{H}^{\mathrm{eb}}$ and $\mathbf{G}^{\mathrm{eb}}$ contain the contributions from collocation points at the external boundary, while $\mathbf{H}^{\mathrm{c}^+}$ and $\mathbf{G}^{\mathrm{c}^+}$ refer to terms from the upper crack face, and $\mathbf{H}^{\mathrm{c}^-}$ and $\mathbf{G}^{\mathrm{c}^-}$ terms from the lower crack face.

As in classical BEM implementations, at this point we can apply a sufficient number of boundary conditions to reduce this to a solvable system. This procedure follows in the same way in IGABEM, but with the modification that a specific treatment is required for the imposition boundary conditions having non-constant value over the patch. A least-square fitting approach is suitable to find the coefficients in a NURBS expansion of the boundary condition. Alternatively, it is possible to directly introduce their analytical expression in the BIEs for patches where they are known, instead of using the NURBS interpolation. Then, the numerical integration takes place by evaluating the applied BC at the integration point, which removes any NURBS functions approximation error. The application in Section 4.3 utilises this alternative procedure in its boundary condition application. After the determination of **d** and **t** coefficients for the known fields, the final algebraic system assumes its form in the usual BEM fashion as:

$$
\mathbf{Ax} = \mathbf{b}
\tag{A.16}
$$

in which **A** contains influence terms associated to the unknowns at the boundary, **x** is the unknown values at the boundary and **b** results from multiplying the prescribed values at the boundary and its correspondent influence terms. It is worth noting that **b** also contains the results of the integration between kernels and BCs when their analytical expression is introduced in the BIE evaluation.

Appendix B. Regularisation of the singular enriched kernels

Boundary integral equations have singular kernels due to the nature of the fundamental solutions. The method adopted for their regularisation is based on the Singularity Subtraction Technique [42,43]. In the XIGABEM context, the new kernels introduced by the expansion of the displacement field for each enrichment strategy herein proposed also inherit this singular behaviour. Thus, SST must be also applied to them, and this is performed by an analogous procedure that consists of considering the augmented basis function as the basis function in the SST. For the Displacement BIE, the strongly singular kernel becomes regular by the expansion in a Taylor Series around the collocation point, which results in evaluating the augmented kernels directly at this position, without requiring any derivatives. On the other hand, the Traction BIE has a hypersingular kernel of order $O(r^{-3})$, which requires the expansion of the basis functions in a Taylor Series to its second term as $\mathbf{\Phi} = \mathbf{\Phi^0}(\hat{\mathbf{x}}) + \rho\mathbf{\Phi^1}(\hat{\mathbf{x}}) + O(\rho^2)$. It is important to mention that the components of $\mathbf{\Phi^1}$ are:

$$\phi^1_\alpha = \frac{\partial \phi_\alpha}{\partial \hat{\xi}_1}\Big|_{\xi_1(\hat{\mathbf{x}}),\xi_2(\hat{\mathbf{x}})} \cos(\theta) + \frac{\partial \phi_\alpha}{\partial \hat{\xi}_2}\Big|_{\xi_1(\hat{\mathbf{x}}),\xi_2(\hat{\mathbf{x}})} \sin(\theta) \tag{B.1}$$

in which θ is the angular value associated to the polar coordinate transformation of the SST. In the context of new kernels, their regularisation takes place by the proper expansion of the enriched basis function in Taylor Series and its further incorporation in the SST expressions. Then, the SST of the arising kernels solely requires the substitution of the standard basis functions and their first derivative by the new augmented basis functions utilised. Therefore, expanding Eq. (B.1) for each enrichment strategy applied in this study is sufficient for SST process.

B.1. Partially cut faces: Williams-based enrichment

For partially cut faces, the $\underline{\mathrm{t}}^{s\,\mathrm{cf}}_{k\ell j}$ kernels of Eq. (7) require regularisation of their $O(r^{-3})$ hypersingular nature. The corresponding augmented basis functions are:

$$\phi^t_{\alpha M} = \phi^\gamma_\alpha R_{kq} \psi^\gamma_{qM} \tag{B.2}$$

and these require expansion in a Taylor series in polar coordinates for the SST, as:

$$\begin{aligned}
\frac{\partial \phi^t_{\alpha M}}{\partial \hat{\xi}_1} &= \frac{\partial \phi^\gamma_\alpha}{\partial \hat{\xi}_1} R_{kq} \psi^\gamma_{qM} + \phi^\gamma_\alpha \frac{\partial R_{kq}}{\partial \hat{\xi}_1} \psi^\gamma_{qM} + \phi^\gamma_\alpha R_{kq} \frac{\partial \psi^\gamma_{qM}}{\partial \hat{\xi}_1} \\
\frac{\partial \phi^t_{\alpha M}}{\partial \hat{\xi}_2} &= \frac{\partial \phi^\gamma_\alpha}{\partial \hat{\xi}_2} R_{kq} \psi^\gamma_{qM} + \phi^\gamma_\alpha \frac{\partial R_{kq}}{\partial \hat{\xi}_2} \psi^\gamma_{qM} + \phi^\gamma_\alpha R_{kq} \frac{\partial \psi^\gamma_{qM}}{\partial \hat{\xi}_2}
\end{aligned} \tag{B.3}$$

in which, for this enrichment, $\frac{\partial R_{kq}}{\partial \hat{\xi}_1} = \frac{\partial R_{kq}}{\partial \hat{\xi}_2} = 0$ since the local coordinate system is fixed at the crack tip. The derivatives of the NURBS basis function are well known from the standard IGABEM, while the derivatives of the enrichment function require further development. Initially, a chain rule enables the derivative in the NURBS parametric space as:

$$\begin{aligned}
\frac{\partial \psi^\gamma_{qM}}{\partial \hat{\xi}_1} &= \frac{\partial \psi^\gamma_{qM}}{\partial \xi_1}\frac{\partial \xi_1}{\partial \hat{\xi}_1} + \frac{\partial \psi^\gamma_{qM}}{\partial \xi_2}\frac{\partial \xi_2}{\partial \hat{\xi}_1} \\
\frac{\partial \psi^\gamma_{qM}}{\partial \hat{\xi}_2} &= \frac{\partial \psi^\gamma_{qM}}{\partial \xi_1}\frac{\partial \xi_1}{\partial \hat{\xi}_2} + \frac{\partial \psi^\gamma_{qM}}{\partial \xi_2}\frac{\partial \xi_2}{\partial \hat{\xi}_2}
\end{aligned} \tag{B.4}$$

but due to the relationship between the parametric space and the Gaussian space, $\frac{\partial \xi_1}{\partial \hat{\xi}_2} = \frac{\partial \xi_2}{\partial \hat{\xi}_1} = 0$. In addition, the Williams-based enrichment function is written in polar coordinates centred at the crack tip. This requires a sequential chain rule for both r^t and θ^t coordinates to obtain the derivatives in the Gaussian space, as:

$$\frac{\partial \psi^\gamma_{qM}}{\partial \hat{\xi}_j} = \frac{\partial \psi^\gamma_{qM}}{\partial r^t}\frac{\partial r^t}{\partial \xi_j}\frac{\partial \xi_j}{\partial \hat{\xi}_j} + \frac{\partial \psi^\gamma_{qM}}{\partial \theta^t}\frac{\partial \theta^t}{\partial \xi_j}\frac{\partial \xi_j}{\partial \hat{\xi}_j} \tag{B.5}$$

for the evaluation of the derivative in respect to the Gaussian coordinate in the j direction and $\frac{\partial \xi_j}{\partial \hat{\xi}_j}$ comes from Eq. (A.9). Furthermore, the derivatives of the Williams enrichment function with respect to the polar coordinates are:

$$\begin{aligned}
\frac{\partial \psi_{qM}}{\partial r^t} &= \frac{1}{2\sqrt{r}}\psi_{qM} \\
\frac{\partial \psi_{nI}}{\partial \theta^t} &= \frac{1}{2\mu}\sqrt{\frac{r^t}{2\pi}}\left\{-\frac{1}{2}\sin\left(\frac{\theta^t}{2}\right)\left[\kappa - 1 + 2\sin^2\left(\frac{\theta^t}{2}\right)\right] + \cos\left(\frac{\theta^t}{2}\right)\sin\theta^t\right\} \\
\frac{\partial \psi_{nII}}{\partial \theta^t} &= \frac{1}{2\mu}\sqrt{\frac{r^t}{2\pi}}\left\{\frac{1}{2}\cos\left(\frac{\theta^t}{2}\right)\left[\kappa + 1 + 2\cos^2\left(\frac{\theta^t}{2}\right)\right] - \sin\left(\frac{\theta^t}{2}\right)\sin\theta^t\right\} \\
\frac{\partial \psi_{bI}}{\partial \theta^t} &= \frac{1}{2\mu}\sqrt{\frac{r^t}{2\pi}}\left\{\frac{1}{2}\cos\left(\frac{\theta^t}{2}\right)\left[\kappa + 1 - 2\cos^2\left(\frac{\theta^t}{2}\right)\right] + \sin\left(\frac{\theta^t}{2}\right)\sin\theta^t\right\} \\
\frac{\partial \psi_{bII}}{\partial \theta^t} &= \frac{1}{2\mu}\sqrt{\frac{r^t}{2\pi}}\left\{\frac{1}{2}\sin\left(\frac{\theta^t}{2}\right)\left[\kappa - 1 - 2\sin^2\left(\frac{\theta^t}{2}\right)\right] + \cos\left(\frac{\theta^t}{2}\right)\sin\theta^t\right\} \\
\frac{\partial \psi_{tIII}}{\partial \theta^t} &= \frac{1}{\mu}\sqrt{\frac{r^t}{2\pi}}\cos\left(\frac{\theta^t}{2}\right)
\end{aligned} \tag{B.6}$$

Lastly, r^t and θ^t are determined based on the position of the crack tip $\mathbf{x}^{\text{ct}}$ as:

$$\begin{aligned}
r^t &= \|\vec{r^t}\| = \sqrt{\sum_{k=1}^{3}(x_k - x_k^{\text{ct}})^2} \\
\theta^t &= \text{sign}\left[(\vec{N}\times\vec{r^t})\cdot\vec{T}\right]\arccos\left(\frac{\vec{N}\cdot\vec{r^t}}{r^t}\right)
\end{aligned} \tag{B.7}$$

in which $\vec{N}$ is the vector parallel to the crack and $\vec{T}$ is the tangent vector, both at the crack tip and obtained by the Frenet–Serret frame. Then, their derivatives in respect to the parametric coordinates are:

$$\begin{aligned}
\frac{\partial r^t}{\partial \xi_j} &= \frac{1}{r^t}\sum_{k=1}^{3}(x_k - x_k^{\text{ct}})\sum_{\alpha=1}^{m}\frac{\partial \phi_\alpha}{\partial \xi_j}P_k^\alpha = \frac{1}{r^t}\sum_{k=1}^{3}(x_k - x_k^{\text{ct}})\frac{\partial \vec{r^t}}{\partial \xi_j} \\
\frac{\partial \theta^t}{\partial \xi_j} &= \frac{-\text{sign}\left[(\vec{N}\times\vec{r^t})\cdot\vec{T}\right]}{\sqrt{1-\left(\frac{\vec{N}\cdot\vec{r^t}}{r^t}\right)^2}}\frac{\vec{N}\cdot\frac{\partial \vec{r^t}}{\partial \xi_j} - \left(\vec{N}\cdot\vec{r^t}\frac{\partial r^t}{\partial \xi_j}\right)}{(r^t)^2}
\end{aligned} \tag{B.8}$$

B.2. Enrichment at the crack front for the direct extraction of SIFs

In the enrichment at the crack front that directly provides the SIFs as unknowns of the XIGABEM system, the local coordinate system is no longer constant over the enriched patch. Additionally, there is a uni-directional function over the crack front to interpolate the additional parameters that are proxiers for the SIFs. In the context of regularising the kernels from Eq. (10), the corresponding augmented basis function is:

$$\phi_{skM}^{\text{cf}} = \tilde{\phi}_s^{\text{cf}}(\upsilon)R_{kq}\psi_{qM}^{\gamma} \tag{B.9}$$

and, for the SST, its first derivative in the Gaussian coordinate direction j becomes:

$$\frac{\partial \phi_{skM}^{\text{cf}}}{\partial \hat{\xi}_j} = \frac{\partial \tilde{\phi}_s^{\text{cf}}}{\partial \hat{\xi}_j}R_{kq}\psi_{qM}^{\gamma} + \tilde{\phi}_s^{\text{cf}}\frac{\partial R_{kq}}{\partial \hat{\xi}_j}\psi_{qM}^{\gamma} + \tilde{\phi}_s^{\text{cf}}R_{kq}\frac{\partial \psi_{qM}^{\gamma}}{\partial \hat{\xi}_j} \tag{B.10}$$

in which both $\tilde{\phi}_s^{\text{cf}}$ and R_{kq} are functions of the uni-direction parametric coordinate t at the crack front. This requires a chain rule in terms of this coordinate as:

$$\begin{aligned}
\frac{\partial \tilde{\phi}_s^{\text{cf}}}{\partial \hat{\xi}_j} &= \frac{d\tilde{\phi}_s^{\text{cf}}}{d\upsilon}\frac{\partial \upsilon}{\partial \xi_j}\frac{\partial \xi_j}{\partial \hat{\xi}_j} \\
\frac{\partial R_{kq}}{\partial \hat{\xi}_j} &= \frac{dR_{kq}}{d\upsilon}\frac{\partial \upsilon}{\partial \xi_j}\frac{\partial \xi_j}{\partial \hat{\xi}_j}
\end{aligned} \tag{B.11}$$

The terms $\frac{d\tilde{\phi}_s^{\text{cf}}}{d\upsilon}$ and $\frac{dR_{kq}}{d\upsilon}$ are the first derivatives of the uni-directional NURBS function and the rotation matrix at the crack front, respectively. In addition, the expression for $\frac{\partial \upsilon}{\partial \xi_j}$ derives from the orthogonality between the vector $\vec{r^t}$ and the tangent vector $\vec{T}$ at the crack front ($\vec{r^t}\cdot\vec{T} = 0$). It is worth mentioning that, for this enrichment, Eq. (B.7) is valid by using x_k^{ct} as $x_k^{\text{cf}}(\upsilon)$ and $\theta^t = \pm\pi$

depending on whether it is a upper or lower crack surface. Then, the first variation of $\vec{r^t} \cdot \vec{T} = 0$ becomes:

$$\begin{aligned} &\delta(\vec{r^t} \cdot \vec{T}) = 0 \Rightarrow \delta\vec{r^t} \cdot \vec{T} + \vec{r^t} \cdot \delta\vec{T} = 0 \Rightarrow \\ &\left(\frac{\partial \vec{r^t}}{\partial \xi_1}\delta\xi_1 + \frac{\partial \vec{r^t}}{\partial \xi_2}\delta\xi_2 + \frac{\partial \vec{r^t}}{\partial v}\delta v \right)\vec{T} + \vec{r^t}\frac{\partial \vec{T}}{\partial v}\delta v = 0 \end{aligned} \tag{B.12}$$

Assuming that $v = v(\xi_1, \xi_2)$, it is possible to write its perturbation in an implicit form as:

$$\delta v = \frac{\partial v}{\partial \xi_1}\delta\xi_1 + \frac{\partial v}{\partial \xi_2}\delta\xi_2 \tag{B.13}$$

which may be substituted into Eq. (B.12) to give:

$$\left[\frac{\partial \vec{r^t}}{\partial \xi_1}\delta\xi_1 + \frac{\partial \vec{r^t}}{\partial \xi_2}\delta\xi_2 + \frac{\partial \vec{r^t}}{\partial v}\left(\frac{\partial v}{\partial \xi_1}\delta\xi_1 + \frac{\partial v}{\partial \xi_2}\delta\xi_2 \right) \right]\vec{T} + \vec{r^t}\frac{\partial \vec{T}}{\partial v}\left(\frac{\partial v}{\partial \xi_1}\delta\xi_1 + \frac{\partial v}{\partial \xi_2}\delta\xi_2 \right) = 0 \tag{B.14}$$

Eq. (B.14) holds for any arbitrary $\delta\xi_i$, $i = 1, 2$. Then, its rearrangement results in:

$$\frac{\partial v}{\partial \xi_i} = \frac{-\frac{\partial \vec{r^t}}{\partial \xi_i} \cdot \vec{T}}{\frac{\partial \vec{r^t}}{\partial v} \cdot \vec{T} + \vec{r^t} \cdot \frac{\partial \vec{T}}{\partial v}} \tag{B.15}$$

Appendix C. Frenet–Serret frame for rotation matrix and derivative

The Frenet–Serret frame relates the rotation matrix and its first derivative with the curve parameterisation, and also the curvature $\kappa(v)$ and torsion $\tau(v)$ properties. In this context, the definition of the rotation system R_{kq} from the tangent vector $\vec{T}$, the normal vector $\vec{N}$ and the bi-normal vector $\vec{B}$ is:

$$\mathbf{R} = \begin{bmatrix} \vec{N} & \vec{B} & \vec{T} \end{bmatrix} \tag{C.1}$$

in which each vector comes from the position $\vec{x}$ in the NURBS curve as:

$$\begin{aligned} \vec{N} &= \frac{\vec{x}' \times (\vec{x}'' \times \vec{x}')}{\|\vec{x}'\| \, \|\vec{x}'' \times \vec{x}'\|} \\ \vec{B} &= \frac{\vec{x}' \times \vec{x}''}{\|\vec{x}' \times \vec{x}''\|} \\ \vec{T} &= \frac{\vec{x}'}{\|\vec{x}'\|} \end{aligned} \tag{C.2}$$

in which $\vec{x}' = \frac{d\vec{x}}{dv}$ and $\vec{x}'' = \frac{d^2\vec{x}}{dv^2}$. The first derivative assumes its form in terms of the rotation matrix $\mathbf{R}$ as:

$$\frac{d\mathbf{R}}{dv} = \|\vec{x}'\| \begin{bmatrix} \vec{N} & \vec{B} & \vec{T} \end{bmatrix} \begin{bmatrix} 0 & -\tau(v) & \kappa(v) \\ \kappa(v) & 0 & 0 \\ -\kappa(v) & 0 & 0 \end{bmatrix} \tag{C.3}$$

Finally, the curvature $\kappa(v)$ and torsion $\tau(v)$ are:

$$\begin{aligned} \kappa(v) &= \frac{\|\vec{x}'' \times \vec{x}'''\|}{\|\vec{x}'\|^3} \\ \tau(v) &= \frac{\vec{x}' \cdot (\vec{x}'' \times \vec{x}''')}{\|\vec{x}' \times \vec{x}''\|^3} \end{aligned} \tag{C.4}$$

with $\vec{x}''' = \frac{d^3\vec{x}}{dv^3}$ as the third derivative of the NURBS curve with respect to the parametric coordinate.

References

[1] J.R. Rice, A path independent integral and the approximate analysis of strain concentration by notches and cracks, J. Appl. Mech. 35 (2) (1968) 379–386, http://dx.doi.org/10.1115/1.3601206.

[2] J. Yau, S. Wang, H. Corten, A mixed-mode crack analysis of isotropic solids using conservation laws of elasticity, J. Appl. Mech. 47 (2) (1980) 335–341, http://dx.doi.org/10.1115/1.3153665.

[3] R. Rigby, M. Aliabadi, Decomposition of the mixed-mode J-integral—revisited, Int. J. Solids Struct. 35 (17) (1998) 2073–2099, http://dx.doi.org/10.1016/S0020-7683(97)00171-6.

[4] S. Chan, I. Tuba, W. Wilson, On the finite element method in linear fracture mechanics, Eng. Fract. Mech. 2 (1) (1970) 1–17, http://dx.doi.org/10.1016/0013-7944(70)90026-3.

[5] J. Martinez, J. Dominguez, On the use of quarter-point boundary elements for stress intensity factor computations, Internat. J. Numer. Methods Engrg. 20 (10) (1984) 1941–1950, http://dx.doi.org/10.1002/nme.1620201013.

[6] S.A. Silling, M. Epton, O. Weckner, J. Xu, E. Askari, Peridynamic states and constitutive modeling, J. Elasticity 88 (2007) 151–184, http://dx.doi.org/10.1007/s10659-007-9125-1.
[7] W. Liu, J.-W. Hong, A coupling approach of discretized peridynamics with finite element method, Comput. Methods Appl. Mech. Engrg. 245 (2012) 163–175, http://dx.doi.org/10.1016/j.cma.2012.07.006.
[8] M.S. Breitenfeld, Quasi-Static Non-Ordinary State-Based Peridynamics for the Modeling of 3D Fracture, University of Illinois at Urbana-Champaign, 2014.
[9] Y. Wang, X. Zhou, Y. Wang, Y. Shou, A 3-D conjugated bond-pair-based peridynamic formulation for initiation and propagation of cracks in brittle solids, Int. J. Solids Struct. 134 (2018) 89–115, http://dx.doi.org/10.1016/j.ijsolstr.2017.10.022.
[10] C. Miehe, M. Hofacker, F. Welschinger, A phase field model for rate-independent crack propagation: Robust algorithmic implementation based on operator splits, Comput. Methods Appl. Mech. Engrg. 199 (45–48) (2010) 2765–2778, http://dx.doi.org/10.1016/j.cma.2010.04.011.
[11] M. Ambati, T. Gerasimov, L. De Lorenzis, A review on phase-field models of brittle fracture and a new fast hybrid formulation, Comput. Mech. 55 (2015) 383–405, http://dx.doi.org/10.1007/s00466-014-1109-y.
[12] G. Molnár, A. Gravouil, 2D and 3D Abaqus implementation of a robust staggered phase-field solution for modeling brittle fracture, Finite Elem. Anal. Des. 130 (2017) 27–38, http://dx.doi.org/10.1016/j.finel.2017.03.002.
[13] P. Diehl, R. Lipton, T. Wick, M. Tyagi, A comparative review of peridynamics and phase-field models for engineering fracture mechanics, Comput. Mech. 69 (6) (2022) 1259–1293, http://dx.doi.org/10.1007/s00466-022-02147-0.
[14] J.T. Oden, C.A. Duarte, Solution of singular problems using hp clouds, Math. Finite Elements Appl. 9 (1996) 35–54.
[15] A.M. Aragón, C.A. Duarte, Fundamentals of Enriched Finite Element Methods, Elsevier, 2024, pp. 275–291, http://dx.doi.org/10.1016/B978-0-32-385515-0.00023-4.
[16] N. Moës, J. Dolbow, T. Belytschko, A finite element method for crack growth without remeshing, Internat. J. Numer. Methods Engrg. 46 (1) (1999) 131–150, http://dx.doi.org/10.1002/(SICI)1097-0207(19990910)46:1<131::AID-NME726>3.0.CO;2-J.
[17] N. Sukumar, N. Moës, B. Moran, T. Belytschko, Extended finite element method for three-dimensional crack modelling, Internat. J. Numer. Methods Engrg. 48 (11) (2000) 1549–1570, http://dx.doi.org/10.1002/1097-0207(20000820)48:11<1549::AID-NME955>3.0.CO;2-A.
[18] C. Duarte, O. Hamzeh, T. Liszka, W. Tworzydlo, A generalized finite element method for the simulation of three-dimensional dynamic crack propagation, Comput. Methods Appl. Mech. Engrg. 190 (15–17) (2001) 2227–2262, http://dx.doi.org/10.1016/S0045-7825(00)00233-4.
[19] P. Laborde, J. Pommier, Y. Renard, M. Salaün, High-order extended finite element method for cracked domains, Internat. J. Numer. Methods Engrg. 64 (3) (2005) 354–381, http://dx.doi.org/10.1002/nme.1370.
[20] P.M. Areias, T. Belytschko, Analysis of three-dimensional crack initiation and propagation using the extended finite element method, Internat. J. Numer. Methods Engrg. 63 (5) (2005) 760–788, http://dx.doi.org/10.1002/nme.1305.
[21] M. Duflot, The extended finite element method in thermoelastic fracture mechanics, Internat. J. Numer. Methods Engrg. 74 (5) (2008) 827–847, http://dx.doi.org/10.1002/nme.2197.
[22] T. Rabczuk, S. Bordas, G. Zi, On three-dimensional modelling of crack growth using partition of unity methods, Comput. Struct. 88 (23–24) (2010) 1391–1411, http://dx.doi.org/10.1016/j.compstruc.2008.08.010.
[23] P. Gupta, C.A. Duarte, Simulation of non-planar three-dimensional hydraulic fracture propagation, Int. J. Numer. Anal. Methods Geomech. 38 (13) (2014) 1397–1430, http://dx.doi.org/10.1002/nag.2305.
[24] H. Talebi, M. Silani, T. Rabczuk, Concurrent multiscale modeling of three dimensional crack and dislocation propagation, Adv. Eng. Softw. 80 (2015) 82–92, http://dx.doi.org/10.1016/j.advengsoft.2014.09.016.
[25] É. Béchet, H. Minnebo, N. Moës, B. Burgardt, Improved implementation and robustness study of the X-FEM for stress analysis around cracks, Internat. J. Numer. Methods Engrg. 64 (8) (2005) 1033–1056, http://dx.doi.org/10.1002/nme.1386.
[26] V. Gupta, C.A. Duarte, I. Babuška, U. Banerjee, A stable and optimally convergent generalized FEM (SGFEM) for linear elastic fracture mechanics, Comput. Methods Appl. Mech. Engrg. 266 (2013) 23–39, http://dx.doi.org/10.1016/j.cma.2013.07.010.
[27] A. Sanchez-Rivadeneira, C. Duarte, A stable generalized/extended FEM with discontinuous interpolants for fracture mechanics, Comput. Methods Appl. Mech. Engrg. 345 (2019) 876–918, http://dx.doi.org/10.1016/j.cma.2018.11.018.
[28] M. Bento, S.P.B. Proença, C. Duarte, Well-conditioned and optimally convergent second-order Generalized/eXtended FEM formulations for linear elastic fracture mechanics, Comput. Methods Appl. Mech. Engrg. 394 (2022) 114917, http://dx.doi.org/10.1016/j.cma.2022.114917.
[29] A. Sanchez-Rivadeneira, N. Shauer, B. Mazurowski, C. Duarte, A stable generalized/extended p-hierarchical FEM for three-dimensional linear elastic fracture mechanics, Comput. Methods Appl. Mech. Engrg. 364 (2020) 112970, http://dx.doi.org/10.1016/j.cma.2020.112970.
[30] A. Sanchez-Rivadeneira, C. Duarte, A simple, first-order, well-conditioned, and optimally convergent Generalized/eXtended FEM for two- and three-dimensional linear elastic fracture mechanics, Comput. Methods Appl. Mech. Engrg. 372 (2020) 113388, http://dx.doi.org/10.1016/j.cma.2020.113388.
[31] H.-K. Hong, J.-T. Chen, Derivations of integral equations of elasticity, J. Eng. Mech. 114 (6) (1988) 1028–1044, http://dx.doi.org/10.1061/(ASCE)0733-9399(1988)114:6(1028).
[32] A. Portela, M. Aliabadi, D. Rooke, The dual boundary element method: effective implementation for crack problems, Internat. J. Numer. Methods Engrg. 33 (6) (1992) 1269–1287, http://dx.doi.org/10.1002/nme.1620330611.
[33] A. Portela, M. Aliabadi, D.P. Rooke, Dual boundary element incremental analysis of crack propagation, Comput. Struct. 46 (2) (1993) 237–247, http://dx.doi.org/10.1016/0045-7949(93)90189-K.
[34] A. Saleh, M. Aliabadi, Crack growth analysis in concrete using boundary element method, Eng. Fract. Mech. 51 (4) (1995) 533–545, http://dx.doi.org/10.1016/0013-7944(94)00301-W.
[35] E.D. Leonel, W.S. Venturini, Dual boundary element formulation applied to analysis of multi-fractured domains, Eng. Anal. Bound. Elem. 34 (12) (2010) 1092–1099, http://dx.doi.org/10.1016/j.enganabound.2010.06.014.
[36] R. Price, J. Trevelyan, Boundary element simulation of fatigue crack growth in multi-site damage, Eng. Anal. Bound. Elem. 43 (2014) 67–75, http://dx.doi.org/10.1016/j.enganabound.2014.03.002.
[37] Y. Mi, M. Aliabadi, Dual boundary element method for three-dimensional fracture mechanics analysis, Eng. Anal. Bound. Elem. 10 (2) (1992) 161–171, http://dx.doi.org/10.1016/0955-7997(92)90047-B.
[38] Y. Mi, M. Aliabadi, Discontinuous crack-tip elements: application to 3D boundary element method, Int. J. Fract. 67 (3) (1994) R67–R71, http://dx.doi.org/10.1007/BF00016267.
[39] A. Cisilino, M. Aliabadi, Three-dimensional boundary element analysis of fatigue crack growth in linear and non-linear fracture problems, Eng. Fract. Mech. 63 (6) (1999) 713–733, http://dx.doi.org/10.1016/S0013-7944(99)00047-8.
[40] K. Kolk, G. Kuhn, The advanced simulation of fatigue crack growth in complex 3D structures, Arch. Appl. Mech. 76 (11) (2006) 699–709, http://dx.doi.org/10.1007/s00419-006-0092-y.
[41] S.G.F. Cordeiro, E.D. Leonel, An improved computational framework based on the dual Boundary Element Method for three-dimensional mixed-mode crack propagation analyses, Adv. Eng. Softw. 135 (2019) 102689, http://dx.doi.org/10.1016/j.advengsoft.2019.102689.
[42] M. Guiggiani, A. Gigante, A general algorithm for multidimensional Cauchy principal value integrals in the Boundary Element Method, J. Appl. Mech. 57 (4) (1990) 906–915, http://dx.doi.org/10.1115/1.2897660.

[43] M. Guiggiani, G. Krishnasamy, T.J. Rudolphi, F.J. Rizzo, A general algorithm for the numerical solution of hypersingular boundary integral equations, J. Appl. Mech. 59 (3) (1992) 604–614, http://dx.doi.org/10.1115/1.2893766.
[44] R. Simpson, J. Trevelyan, A partition of unity enriched dual boundary element method for accurate computations in fracture mechanics, Comput. Methods Appl. Mech. Engrg. 200 (1–4) (2011) 1–10, http://dx.doi.org/10.1016/j.cma.2010.06.015.
[45] R. Simpson, J. Trevelyan, Evaluation of J1 and J2 integrals for curved cracks using an enriched boundary element method, Eng. Fract. Mech. 78 (4) (2011) 623–637, http://dx.doi.org/10.1016/j.engfracmech.2010.12.006.
[46] I. Alatawi, J. Trevelyan, A direct evaluation of stress intensity factors using the extended dual boundary element method, Eng. Anal. Bound. Elem. 52 (2015) 56–63, http://dx.doi.org/10.1016/j.enganabound.2014.11.022.
[47] G. Hattori, I.A. Alatawi, J. Trevelyan, An extended boundary element method formulation for the direct calculation of the stress intensity factors in fully anisotropic materials, Internat. J. Numer. Methods Engrg. 109 (7) (2017) 965–981, http://dx.doi.org/10.1002/nme.5311.
[48] H.C. Andrade, E.D. Leonel, An enriched dual boundary element method formulation for linear elastic crack propagation, Eng. Anal. Bound. Elem. 121 (2020) 158–179, http://dx.doi.org/10.1016/j.enganabound.2020.09.007.
[49] I. Alatawi, Extended Boundary Element Method approach for Direct and Accurate Evaluation of Stress Intensity Factors (Ph.D. thesis), Durham University, 2016.
[50] T. Hughes, J. Cottrell, Y. Bazilevs, Isogeometric analysis: CAD, finite elements, NURBS, exact geometry and mesh refinement, Comput. Methods Appl. Mech. Engrg. 194 (39) (2005) 4135–4195, http://dx.doi.org/10.1016/j.cma.2004.10.008.
[51] M.J. Borden, T.J. Hughes, C.M. Landis, C.V. Verhoosel, A higher-order phase-field model for brittle fracture: Formulation and analysis within the isogeometric analysis framework, Comput. Methods Appl. Mech. Engrg. 273 (2014) 100–118, http://dx.doi.org/10.1016/j.cma.2014.01.016.
[52] J. Kiendl, M. Ambati, L. De Lorenzis, H. Gomez, A. Reali, Phase-field description of brittle fracture in plates and shells, Comput. Methods Appl. Mech. Engrg. 312 (2016) 374–394, http://dx.doi.org/10.1016/j.cma.2016.09.011.
[53] N. Nguyen-Thanh, W. Li, J. Huang, K. Zhou, Multi phase-field modeling of anisotropic crack propagation in 3D fiber-reinforced composites based on an adaptive isogeometric meshfree collocation method, Comput. Methods Appl. Mech. Engrg. 393 (2022) 114794, http://dx.doi.org/10.1016/j.cma.2022.114794.
[54] D.J. Benson, Y. Bazilevs, E. De Luycker, M.-C. Hsu, M. Scott, T. Hughes, T. Belytschko, A generalized finite element formulation for arbitrary basis functions: from isogeometric analysis to XFEM, Internat. J. Numer. Methods Engrg. 83 (6) (2010) 765–785, http://dx.doi.org/10.1002/nme.2864.
[55] E. De Luycker, D.J. Benson, T. Belytschko, Y. Bazilevs, M.C. Hsu, X-FEM in isogeometric analysis for linear fracture mechanics, Internat. J. Numer. Methods Engrg. 87 (6) (2011) 541–565, http://dx.doi.org/10.1002/nme.3121.
[56] C.V. Verhoosel, M.A. Scott, R. De Borst, T.J. Hughes, An isogeometric approach to cohesive zone modeling, Internat. J. Numer. Methods Engrg. 87 (1–5) (2011) 336–360, http://dx.doi.org/10.1002/nme.3061.
[57] S.S. Ghorashi, N. Valizadeh, S. Mohammadi, Extended isogeometric analysis for simulation of stationary and propagating cracks, Internat. J. Numer. Methods Engrg. 89 (9) (2012) 1069–1101, http://dx.doi.org/10.1002/nme.3277.
[58] S.S. Ghorashi, N. Valizadeh, S. Mohammadi, T. Rabczuk, T-spline based XIGA for fracture analysis of orthotropic media, Comput. Struct. 147 (2015) 138–146, http://dx.doi.org/10.1016/j.compstruc.2014.09.017.
[59] N. Nguyen-Thanh, N. Valizadeh, M. Nguyen, H. Nguyen-Xuan, X. Zhuang, P. Areias, G. Zi, Y. Bazilevs, L. De Lorenzis, T. Rabczuk, An extended isogeometric thin shell analysis based on Kirchhoff–Love theory, Comput. Methods Appl. Mech. Engrg. 284 (2015) 265–291, http://dx.doi.org/10.1016/j.cma.2014.08.025.
[60] R. Simpson, S. Bordas, J. Trevelyan, T. Rabczuk, A two-dimensional isogeometric boundary element method for elastostatic analysis, Comput. Methods Appl. Mech. Engrg. 209–212 (2012) 87–100, http://dx.doi.org/10.1016/j.cma.2011.08.008.
[61] M. Scott, R. Simpson, J. Evans, S. Lipton, S. Bordas, T. Hughes, T. Sederberg, Isogeometric boundary element analysis using unstructured T-splines, Comput. Methods Appl. Mech. Engrg. 254 (2013) 197–221, http://dx.doi.org/10.1016/j.cma.2012.11.001.
[62] G. Beer, B. Marussig, C. Duenser, The Isogeometric Boundary Element Method, Springer, 2020.
[63] H.C. Andrade, J. Trevelyan, E.D. Leonel, A NURBS-discontinuous and enriched isogeometric boundary element formulation for two-dimensional fatigue crack growth, Eng. Anal. Bound. Elem. 134 (2022) 259–281, http://dx.doi.org/10.1016/j.enganabound.2021.09.019.
[64] H.C. Andrade, J. Trevelyan, E.D. Leonel, Direct evaluation of stress intensity factors and T-stress for bimaterial interface cracks using the extended isogeometric boundary element method, Theor. Appl. Fract. Mech. (2023) 104091, http://dx.doi.org/10.1016/j.tafmec.2023.104091.
[65] E. Atroshchenko, S. Tomar, G. Xu, S.P. Bordas, Weakening the tight coupling between geometry and simulation in isogeometric analysis: From sub-and super-geometric analysis to Geometry-Independent Field approximaTion (GIFT), Internat. J. Numer. Methods Engrg. 114 (10) (2018) 1131–1159.
[66] B. Marussig, J. Zechner, G. Beer, T.-P. Fries, Fast isogeometric boundary element method based on independent field approximation, Comput. Methods Appl. Mech. Engrg. 284 (2015) 458–488.
[67] G. Beer, B. Marussig, J. Zechner, A simple approach to the numerical simulation with trimmed CAD surfaces, Comput. Methods Appl. Mech. Engrg. 285 (2015) 776–790.
[68] G. Beer, B. Marussig, J. Zechner, C. Dünser, T.-P. Fries, Isogeometric boundary element analysis with elasto-plastic inclusions. Part 1: plane problems, Comput. Methods Appl. Mech. Engrg. 308 (2016) 552–570.
[69] G. Beer, V. Mallardo, E. Ruocco, B. Marussig, J. Zechner, C. Dünser, T.-P. Fries, Isogeometric boundary element analysis with elasto-plastic inclusions. Part 2: 3-D problems, Comput. Methods Appl. Mech. Engrg. 315 (2017) 418–433.
[70] G. Beer, V. Mallardo, E. Ruocco, C. Dünser, Isogeometric boundary element analysis of steady incompressible viscous flow, part 1: Plane problems, Comput. Methods Appl. Mech. Engrg. 326 (2017) 51–69.
[71] W. Zhou, B. Liu, Q. Wang, Y. Cheng, G. Ma, X. Chang, X. Chen, NURBS-enhanced boundary element method based on independent geometry and field approximation for 2D potential problems, Eng. Anal. Bound. Elem. 83 (2017) 158–166.
[72] X. Peng, E. Atroshchenko, P. Kerfriden, S.P.A. Bordas, Isogeometric boundary element methods for three dimensional static fracture and fatigue crack growth, Comput. Methods Appl. Mech. Engrg. 316 (2017) 151–185, http://dx.doi.org/10.1016/j.cma.2016.05.038.
[73] S.G.F. Cordeiro, E.D. Leonel, Mechanical modelling of three-dimensional cracked structural components using the isogeometric dual boundary element method, Appl. Math. Model. 63 (2018) 415–444, http://dx.doi.org/10.1016/j.apm.2018.06.042.
[74] F. Sun, C. Dong, Three-dimensional crack propagation and inclusion-crack interaction based on IGABEM, Eng. Anal. Bound. Elem. 131 (2021) 1–14, Three-dimensional crack propagation and inclusion-crack interaction based on IGABEM.
[75] F. Sun, C. Dong, Effective elastic properties of three-dimensional multiple crack problems with the isogeometric boundary element parallel fast direct solver, Eng. Anal. Bound. Elem. 155 (2023) 1104–1122, http://dx.doi.org/10.1016/j.enganabound.2023.07.038.
[76] C. He, X. Peng, C. Ding, Dual order-reduced Gaussian process emulators (DORGP) for quantifying high-dimensional uncertain crack growth using limited and noisy data, Comput. Methods Appl. Mech. Engrg. 417 (2023) http://dx.doi.org/10.1016/j.cma.2023.116394.
[77] T. Belytschko, N. Moës, S. Usui, C. Parimi, Arbitrary discontinuities in finite elements, Internat. J. Numer. Methods Engrg. 50 (4) (2001) 993–1013, http://dx.doi.org/10.1002/1097-0207(20010210)50:4<993::aid-nme164>3.0.co;2-m.
[78] M. Williams, On the stress distribution at the base of a stationary crack, J. Appl. Mech. 24 (1) (1957) 109–114, http://dx.doi.org/10.1115/1.4011454.
[79] C. Duarte, I. Babuška, J. Oden, Generalized finite element methods for three-dimensional structural mechanics problems, Comput. Struct. 77 (2) (2000) 215–232, http://dx.doi.org/10.1016/s0045-7949(99)00211-4.

[80] L. Piegl, W. Tiller, The NURBS Book, Springer Science & Business Media, 1996, http://dx.doi.org/10.1007/978-3-642-59223-2.
[81] F. Frenet, Sur les courbes à double courbure, J. Math. Pures Appl. 17 (1852) 437–447.
[82] J.-A. Serret, Sur quelques formules relatives à la théorie des courbes à double courbure, J. Math. Pures Appl. 16 (1851) 193–207.
[83] S. Li, M. Mear, L. Xiao, Symmetric weak-form integral equation method for three-dimensional fracture analysis, Comput. Methods Appl. Mech. Engrg. 151 (3) (1998) 435–459, http://dx.doi.org/10.1016/S0045-7825(97)00199-0, Containing papers presented at the Symposium on Advances in Computational Mechanics.
[84] C. Brebbia, The Boundary Element Method for Engineers, Pentech Press, 1978.
[85] H. Tada, P. Paris, G. Irwin, The Analysis of Cracks Handbook, vol. 2, ASME Press, New York, 2000, p. 1.
[86] S.A. Sauter, C. Schwab, Boundary Element Methods, Springer, 2011.
[87] B. Marussig, R. Hiemstra, T.J. Hughes, Improved conditioning of isogeometric analysis matrices for trimmed geometries, Comput. Methods Appl. Mech. Engrg. 334 (2018) 79–110.
[88] M.G. Cox, The numerical evaluation of B-splines*, IMA J. Appl. Math. 10 (2) (1972) 134–149, http://dx.doi.org/10.1093/imamat/10.2.134.
[89] C. De Boor, On calculating with B-splines, J. Approx. Theory 6 (1) (1972) 50–62, http://dx.doi.org/10.1016/0021-9045(72)90080-9.
[90] C. De Boor, A Practical Guide To Splines, vol. 27, Springer-Verlag New York, 1978, http://dx.doi.org/10.1007/978-1-4612-6333-3.
[91] T. Greville, Numerical procedures for interpolation by spline functions, J. Soc. Ind. Appl. Math. B Numer. Anal. 1 (1) (1964) 53–68, http://dx.doi.org/10.1137/0701005.